PE&RS
April 2023 Volume 89, Number 4
Photogrammetric Engineering & Remote Sensing The official journal for imaging and geospatial information science and technology

2023 ASPRS International Technical Symposium

June 12-16, 2023
VIRTUAL

ASPRS is happy to announce the dates of its virtual conference. The 2023 ASPRS International Technical Symposium will take place.

The symposium will consist of:

- 15-minute oral presentations
- 5-minute Ignite-style presentations
- Poster Gallery
- Sustaining Member Vendor Spotlights
- ASPRS Society Highlights

Sessions will run each day from 10:00 AM to 6:00 PM Eastern Daylight Time (UTC - 4). All sessions will be recorded and made available on-demand to conference registrants. Presenters are eligible to submit full manuscripts for publication in the ISPRS Archives.

Interested in Presenting? For more information or to submit an abstract visit https://my.asprs.org/2023Symposium/2023-Symposium/Call-for-Abstracts.aspx

- Submission deadline is May 1, 2023
- Presenters will be notified of acceptance by May 8, 2023
- Presenters must be registered for the conference by May 22, 2023 to be included in the conference program

Registration Fees

• ASPRS Member	$150 USD
• ASPRS Student Member	$ 50 USD
• ASPRS Emeritus Member	$ 25 USD
• Non Member	$250 USD

Sponsorship Opportunities

- Vendor Spotlight/Product Demo
- Day Sponsor
- Session Sponsor
- Workshop Sponsor

"We are happy to offer this educational opportunity to the geospatial community. Virtual events are an excellent way to exchanammunity without the cost and time constraints of travel," said Karen Schuckman, ASPRS Executive Director

https://my.asprs.org/2023Symposium/

ANNOUNCEMENTS

2023 William T. Pecora Award Nominations Now Being Accepted through May 1, 2023—The William T. Pecora Award is presented annually to individuals or groups who have made outstanding contributions toward understanding the Earth by means of remote sensing. The Department of the Interior (DOI) and the National Aeronautics and Space Administration (NASA) jointly sponsor the award.

The award was established in 1974 to honor the memory of Dr. William T. Pecora, former Director of the U.S. Geological Survey and Under Secretary, Department of the Interior. Dr. Pecora was a motivating force behind the establishment of a program for civil remote sensing of the Earth from space. His early vision and support helped establish what we know today as the Landsat satellite program.

The Award Committee must receive nominations for the 2023 award by May 1, 2023. Additional information can be found at www.usgs.gov/pecora or on the attached flyer; and questions can be directed to the Executive Secretary and Committee at pecora@usgs.gov.

Esri, the global leader in geographic information system (GIS) and location intelligence, honored select partners for their outstanding application of GIS software during the Plenary session at the Esri Partner Conference (EPC) held at the Palm Springs Convention Center in Palm Springs, CA. The award-winning companies are organizations in the Esri Partner Network and are recognized for their innovation and excellence in helping customers succeed with ArcGIS technology.

EPC award categories and winners include the following:

Analytics to Insights Award—*Delivering analytics and insights to users through location intelligence*: **Dewberry** and StreetLight Data.

ArcGIS Marketplace Award—*Outstanding presence on ArcGIS Marketplace*: VertiGIS North America.

ArcGIS SaaS Adoption Award—*Evolving customers and solutions to ArcGIS using SaaS*: Pandell Technology and Pro-West & Associates.

ArcGIS Software Adoption Award—*Demonstrating highly-aligned solutions built with ArcGIS software products*: Arora Engineers and Geo Data AG.

Cloud System Implementation Award—*Ensuring customer success through comprehensive implementation of the ArcGIS system in the cloud*: Axim Geospatial and ROK Technologies.

Creative Content Award—*Delivering creative content to ArcGIS users*: **Nearmap** and **Vexcel Imaging**.

GIS for Diversity Award—*Leveraging GIS in service to diversity, equity, inclusion, and belonging*: GISetc, a division of Critical Think and Timmons Group.

GIS for Good Award—*Compelling use of Esri technology to make an impact on current issues around the world*: Dymaptic and Nelson Intelligence Solutions.

Innovation Award—*Use of ArcGIS system in an innovative or disruptive way*: Houseal Lavigne and vGIS

Partner-to-Partner Collaboration Award—*Innovative technical or business collaboration between partners*: Datastory, GeoMarvel, and SymGEO.

Sustainable Development Award—*Helping customers meet global sustainable development goals by understanding their needs, mapping their work, measuring impact, analyzing performance, and engaging stakeholders*: Blue Raster and Codex Remote.

Top Co-Sell Partner Award—*Positively influences the adoption of Esri technology through solution sales, software implementation, and/or consulting engagements*: Geographic Technologies and SSP Innovations.

Top Solution Partner Award—*Drives the use of Esri technology through the sales of commercial solutions*: Motorola Solutions and VertiGIS GmbH.

Top Startup Partner Award—*Substantial opportunities for growth with Esri*: ICEYE.

The Esri Partner Conference was held March 4–6, 2023. During this event, organizations in the Esri partner community collaborate and network, hear about Esri's vision and new opportunities, build business relationships, learn from Esri experts, exchange ideas, discover the latest technology releases, and make plans for growing their businesses.

To learn more about the Esri Partner Network, visit go.esri.com/EsriPartnerNetwork.

Woolpert was a huge winner at the annual Geo Week conference in Denver, taking home multiple top awards. Geo Week combines the International Lidar Mapping Forum, SPAR 3D Expo & Conference, and AEC Next conferences to provide the geospatial industry's keystone event.

Literally chief among those honored was Woolpert Vice President and Chief Scientist Qassim Abdullah, who received the Lidar Leader Outstanding Personal Achievement Award. In addition to helping write standards upon which the industry is based, Abdullah serves as an advisor for agencies like NOAA and the Transportation Research Board, teaches

graduate students at Penn State University and the University of Maryland Baltimore County, and writes a monthly ***Mapping Matters Column*** for the ***PE&RS***. Through these and countless other efforts, Abdullah continues to advance the lidar industry. He has been an immensely valued leader at Woolpert for more than 10 years.

Woolpert also received the Lidar Leader Outstanding Innovation in Lidar Award. The award was for the firm's Bathymetric Unmanned Littoral LiDar for Operational GEOINT technologies and sensor, also known as BULLDOG. Woolpert was granted a U.S. patent for its "Airborne Topo-Bathy Lidar System and Methods Thereof," and a lidar sensor system was developed by a multidisciplinary research and development team incorporating these technologies. These technologies enable the collection of high-resolution topographic and bathymetric data at a higher altitude, resulting in a broader swath than previously developed lidar systems. The Joint Airborne Lidar Bathymetry Technical Center of Expertise (JALBTCX) contracted with Woolpert to develop BULLDOG.

"Commercially available airborne lidar bathymetry systems currently operate at low altitudes, which are far below the altitudes of topographic lidar systems," Woolpert Vice President Nathan Hopper said. "Increasing the operational altitude of airborne lidar bathymetry systems to 10,000 feet presented several challenges that required novel approaches. This patent covers the proprietary technology developed to overcome the many challenges associated with high-altitude topography and bathymetry."

Hopper, Woolpert Senior Vice President and Geospatial Leader Joseph Seppi, Woolpert Vice President Mark Smits, and Chris Macon, a physical scientist for the U.S. Army Corps of Engineers, were instrumental to this technology and were on hand to accept the award. Collaboration with JALBTCX was key to this groundbreaking technology.

Woolpert also was honored with the MAPPS Membership Choice Award for a project that involved mission-critical data delivery for geohazard defense in Barry Arm, Alaska. The award recognized the work of eTrac, a Woolpert Company, and its immediate response to emergency request from U. S. Geological Survey and the Alaska Division of Geological and Geophysical Surveys.

The team acquired and expedited the delivery of bathymetric survey data to support accurate modeling of the seafloor and the region's steep continental slope, which was at risk for tsunami-generating submarine landslides that could lead to catastrophic loss of life and property. Woolpert Senior Vice President Jeff Lovin accepted the award on behalf of Woolpert Market Director and Certified Hydrographer Dave Neff.

Finally, Woolpert Vice President and Survey Discipline Leader David Kuxhausen received the **ASPRS Outstanding Service Award**. Kuxhausen's experience in photogrammetric and geodetic surveys, UAS data collection and analysis, and mobile lidar applications is unparalleled. He has been an outstanding leader and mentor at Woolpert for 24 years.

Request for Public Comment on a Draft Standard Ocean Mapping Protocol—The National Ocean Mapping, Exploration, and Characterization (NOMEC) Council and the Interagency Working Group on Ocean and Coastal Mapping (IWG-OCM) request public comment from all interested parties on the IWG-OCM's draft Standard Ocean Mapping Protocol (SOMP). The draft SOMP was developed in accordance with Objective 2.1 of the National Strategy for Ocean Mapping, Exploring, and Characterizing the United States Exclusive Economic Zone (National Strategy). Objective 2.1 directs the IWG-OCM to establish a SOMP to encourage consistency in data acquisition, stewardship and data management across a subset of ocean sensing capabilities for seafloor mapping, including bathymetry (acoustic and airborne), seabed backscatter, water column backscatter, side scan sonar imagery, sub-bottom profiling, and magnetometer data readings.

Comments must be received via email by 5:00 PM (ET) on June 2, 2023.

https://www.federalregister.gov/documents/2023/02/24/2023-03795/request-for-public-comment-on-a-draft-standard-ocean-mapping-protocol.

CALENDAR

- 5 May, **ASPRS GeoByte — SeaSketch 2.0: A New, Free and Open Source software Service for Map-based Surveys and Collaborative Geodesign.** For more information, visit https://www.asprs.org/geobytes.html.
- 12-16 June, **ASPRS 2023 International Technical Symposium.** For more information, visit https://my.asprs.org/2023Symposium/.
- 16-19 October, **GIS-Pro 2023**, Columbus, Ohio. For more information, visit www.urisa.org/gis-pro.

PE&RS
PHOTOGRAMMETRIC ENGINEERING & REMOTE SENSING
The official journal for imaging and geospatial information science and technology
April 2023 Volume 89 Number 4

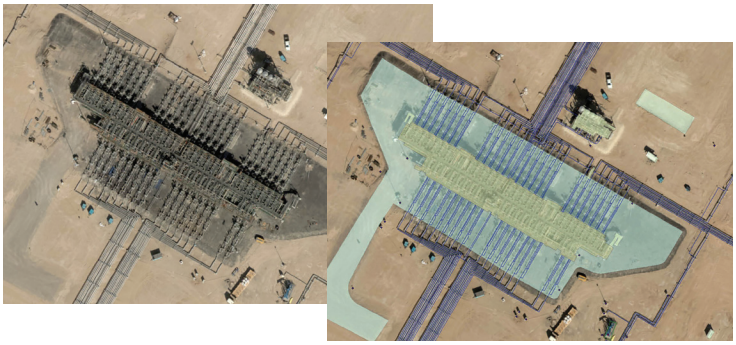

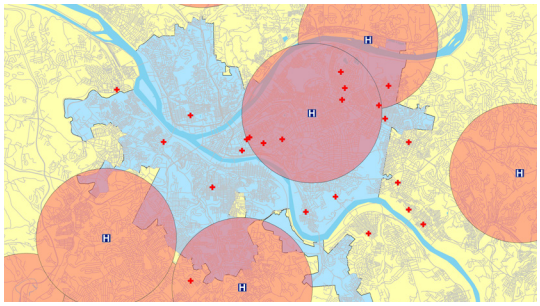

197 **Mapping Kuwait Oil Company's Assets using Photogrammetry Techniques**
By Adnan Dashti, Faisal Al-Bous, Fahad Al Ajmi, Nasser Al Ajmi, Nasir Osman, and Ramesh Mahishi V Murthy

203 **GIS Tips & Tricks — Buffers Everywhere but Where You Want Them?**

COLUMNS

203 GIS Tips & Tricks — Buffers Everywhere but Where You Want Them?

205 SectorInsight.org — Great Lakes Remote Sensing: Binational, Petascale, Wetlands and Habitats Change Mapping

ANNOUNCEMENTS

209 Headquarters News

209 New ASPRS Members
Join us in welcoming our newest members to ASPRS.

210 ASPRS GeoByte — SeaSketch 2.0: A New, Free and Open-source Software Service for Map-based Surveys and Collaborative Geodesign

244 Call for *PE&RS* Special Issue Submissions — Innovative Methods for Geospatial Data using Remote Sensing and GIS

DEPARTMENTS

193 Industry News

194 Calendar

220 In-Press *PE&RS* Articles

259 Who's Who in ASPRS

260 ASPRS Sustaining Members

211 A GPU-Accelerated PCG Method for the Block Adjustment of Large-Scale High-Resolution Optical Satellite Imagery Without GCPs
Qing Fu, Xiaohua Tong, Shijie Liu, Zhen Ye, Yanmin Jin, Hanyu Wang, and *Zhonghua Hong*

The precise geo-positioning of high-resolution satellite imagery (HRSI) without ground control points (GCPs) is an important and fundamental step in global mapping, three-dimensional modeling. In this article, to improve the efficiency of large-scale bundle adjustment (BA), we propose a combined Preconditioned Conjugate Gradient (PCG) and Graphic Processing Unit (GPU) parallel computing approach for the BA of large-scale HRSI without GCPs.

221 Identification of Drought Events in Major Basins of Africa from GRACE Total Water Storage and Modeled Products
Ayman M. Elameen, Shuanggen Jin, and *Daniel Olago*

Terrestrial water storage (TWS) plays a vital role in climatological and hydrological processes. Most of the developed drought indices from the Gravity Recovery and Climate Experiment (GRACE) over Africa neglected the influencing roles of individual water storage components in calculating the drought index and thus may either underestimate or overestimate drought characteristics. In this article, we proposed a Weighted Water Storage Deficit Index for drought assessment over the major river basins in Africa (i.e., Nile, Congo, Niger, Zambezi, and Orange) with accounting for the contribution of each TWS component on the drought signal.

233 Lightweight Parallel Octave Convolutional Neural Network for Hyperspectral Image Classification
Dan Li, Hanjie Wu, Yujian Wang, Xiaojun Li, Fanqiang Kong, and *Qiang Wang*

Although most deep learning-based methods have achieved excellent performance for hyperspectral image (HSI) classification, they are often limited by complex networks and require massive training samples in practical applications. Therefore, designing an efficient, lightweight model to obtain better classification results under small samples situations remains a challenging task. To alleviate this problem, a novel, lightweight parallel octave convolutional neural network (LPOCNN) for HSI classification is proposed in this article.

245 Model-Driven Precise Degradation Analysis Method of Highway Marking Using Mobile Laser Scanning Point Clouds
Ruifeng Ma, Xuming Ge, Qing Zhu, Xin Jia, Huiwei Jiang, Min Chen, and *Tao Liu*

Highway markings (HMs) are representative elements of inventory digitalization in highway scenes. The accurate position, semantics, and maintenance information of HMs provide significant support for the intelligent management of highways. This article presents a robust and efficient approach for extracting, reconstructing, and degrading analyzing HMs in complex highway scenes.

See the Cover Description on Page 196

COVER DESCRIPTION

As early as the 1930s, researchers noticed that odd, milky-white patches of water sporadically discolor the generally bluer and shallow waters of the Bahama Banks. Sampling the discolored water patches made clear that these whiting events were caused by an abundance of fine-grained calcium carbonate particles suspended in the water.

However, why surges of calcium carbonate end up suspended in the water at particular times has never been clear. Some experts have argued that it is mainly a mechanical process, with currents dredging up calcium carbonate sediments. Others have proposed that phytoplankton blooms and other biological or chemical processes might be key to triggering whiting events.

"But in actuality, there is no scientific consensus on what cause them," explained Chuanmin Hu, an oceanographer at the University of South Florida.

The Operational Land Imager (OLI) on Landsat 8 captured this natural-color image of a whiting event off the west coast of Great Bahama Bank on April 4, 2015. The bright spots—whitings—are surrounded by shallow water. Whiting events generally persist for a few days to three months; the event shown here lasted for about two months before fading away.

In a recent attempt to better understand what causes whiting events, a team of University of South Florida researchers, led by Hu, developed a machine learning model that analyzed thousands of satellite images of the Bahama Banks collected by NASA's Aqua satellite between 2003-2020. In doing so, the research team assembled the longest and most detailed monthly, seasonal, and annual records of Bahama Bank whiting events ever created, according to Hu. The results were recently published in *Remote Sensing of Environment*.

The researchers reported stark seasonal patterns in the timing of whiting events, with significantly more of them happening in the spring and winter. They found large variations in the size of individual whiting patches, from 0.1 to 226 square kilometers, with the average size being 2.4 square kilometers for the Great Bahama Bank, roughly the size of 450 American football fields.

Most striking, the team observed what they termed a "mysterious" increase in the total area affected by whiting events, which rose from an average of about 25 square kilometers in 2003 to as much as 300-350 square kilometers in 2014-2015. After 2015, the total area affected began to decline gradually, returning to about 25 square kilometers by 2020. The cover image shows an event during the peak of whiting activity in January 2015.

"I wish I could tell you why we saw that peak in activity, but we're not there yet," said Hu. "We do see some interesting relationships between environmental conditions, such as the pH, the salinity of water, and the behavior of winds and currents, but we can't yet say what exact mechanical, biological, or chemical processes were responsible for that peak in activity. Ultimately, we need to do more field experiments and pair that with remote sensing research like this to better understand the formation processes."

For more information, visit https://landsat.visibleearth.nasa.gov/view.php?id=150866.

NASA Earth Observatory image by Joshua Stevens, using Landsat data from the U.S. Geological Survey. Story by Adam Voiland.

PHOTOGRAMMETRIC ENGINEERING & REMOTE SENSING

JOURNAL STAFF

Publisher ASPRS
Editor-In-Chief Alper Yilmaz
Director of Publications Rae Kelley
Electronic Publications Manager/Graphic Artist
Matthew Austin

Photogrammetric Engineering & Remote Sensing is the official journal of the American Society for Photogrammetry and Remote Sensing. It is devoted to the exchange of ideas and information about the applications of photogrammetry, remote sensing, and geographic information systems. The technical activities of the Society are conducted through the following Technical Divisions: Geographic Information Systems, Photogrammetric Applications, Lidar, Primary Data Acquisition, Professional Practice, Remote Sensing Applications, and Unmanned Autonomous Systems. Additional information on the functioning of the Technical Divisions and the Society can be found in the Yearbook issue of *PE&RS*.

All written correspondence should be directed to the American Society for Photogrammetry and Remote Sensing, PO Box 14713, Baton Rouge, LA 70898, including general inquiries, memberships, subscriptions, business and editorial matters, changes in address, manuscripts for publication, advertising, back issues, and publications. The telephone number of the Society Headquarters is 301-493-0290; the fax number is 225-408-4422; web address is www.asprs.org.

PE&RS. *PE&RS* (ISSN0099-1112) is published monthly by the American Society for Photogrammetry and Remote Sensing, 8550 United Plaza Blvd, Suite 1001, Baton Rouge, Louisiana 70809 . Periodicals postage paid at Bethesda, Maryland and at additional mailing offices.

SUBSCRIPTION. *PE&RS* is available as an e-Subscription (single-site and multi-site licenses) and an e-Subscription with print add-on (single-site license only). PE&RS subscriptions are on a calendar-year, beginning in January and ending in December.

The rate for a single-site e-Subscription for the USA/Non-USA is $1040 USD, for Canadian* is $1092 USD.

The rate for a multi-site e-Subscription for the USA/Non-USA is $1040 USD plus $250 USD for each additional license, for Canadian* is $1092 USD plus $263 for each additional license.

The rate for e-Subscription with print add-on for the USA is $1525 USD, for Canadian* is $1612 USD, and for Non-USA is $1565 USD.

*Note: Subscription prices for Canada includes 5% of the total amount for Canada's Goods and Services Tax (GST #135123065). **PLEASE NOTE: All Subscription Agencies receive a 20.00 USD discount.**

POSTMASTER. Send address changes to PE&RS, ASPRS, PO Box 14713, Baton Rouge, LA 70898. CDN CPM #(40020812).

MEMBERSHIP. Membership is open to any person actively engaged in the practice of photogrammetry, photointerpretation, remote sensing and geographic information systems; or who by means of education or profession is interested in the application or development of these arts and sciences. Membership is for one year, with renewal based on the anniversary date of the month joined. Membership Dues include a 12-month electronic subscription to *PE&RS*. Annual Individual Membership dues are $150.00 USD and Student Membership dues are $50.00 USD. A tax of 5% for Canada's Goods and Service Tax (GST #135123065) is applied to all members residing in Canada.

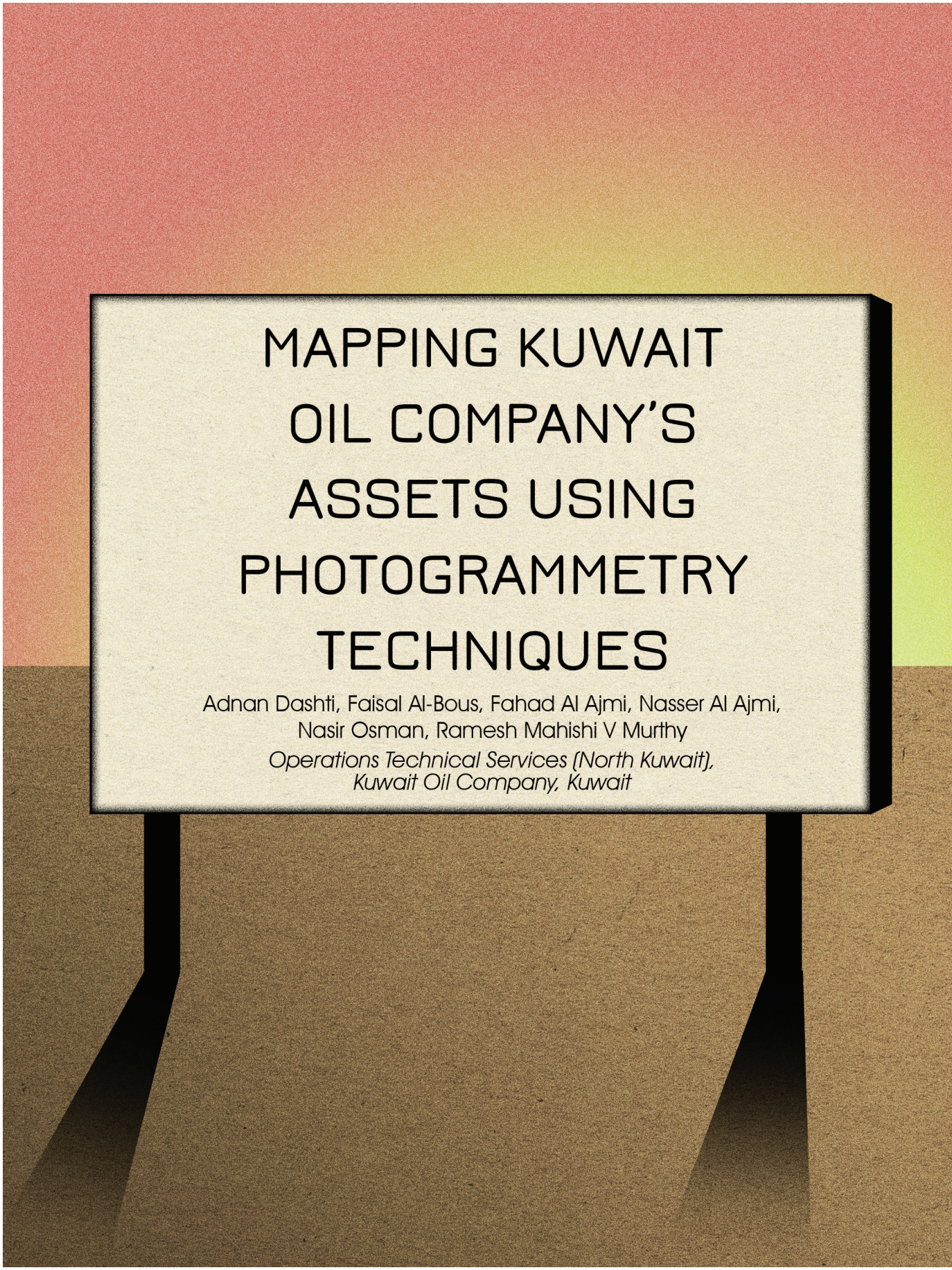

MAPPING KUWAIT OIL COMPANY'S ASSETS USING PHOTOGRAMMETRY TECHNIQUES

Adnan Dashti, Faisal Al-Bous, Fahad Al Ajmi, Nasser Al Ajmi, Nasir Osman, Ramesh Mahishi V Murthy

Operations Technical Services (North Kuwait), Kuwait Oil Company, Kuwait

Introduction

The Infrastructure Master Plan (IMP) of the Operations Support Group, Kuwait Oil Company (KOC) is responsible for developing a Master Plan to manage the oil field's surface footprint. IMP produces and maintains the data used for planning, operations and Health, Safety & Environment (HSE) activities. IMP primarily uses the data from land survey to create a basemap. However, areas that are hazardous and inaccessible to surveyors create data voids. IMP supplements the missing details with data compiled using photogrammetry techniques. IMP utilizes DATEM Summit Evolution with ArcGIS and ArcGIS Pro for stereo visualization and photogrammetry data compilation.

Mapping Approach

Aerial data acquisition for photogrammetry data compilation was performed using Leica RCD 30 Digital Imagery Sensor mounted on a Rockwell International 690A aircraft. The details of Aerial acquisition of the project were published in Photogrammetric Engineering & Remote Sensing, Vol. 87, No. 5, May 2021, pp. 313-317, DOI: 10.14358/PERS.87.5.313.

Mapping KOC assets involves coincident activities such as land survey and photogrammetry data compilation which were carefully planned so there were not duplication of effort or areas creating data voids. KOC fully understands that the utilities within inaccessible areas cannot be mapped by land surveyors. For instance, the extents of oil lakes which were created due to oil spills from the invasion of Iraq, the vital KOC assets within oil lake boundaries, etc., the access to which could pose life threatening risks to land surveyors.

Challenges during Photogrammetry Data Compilation

The industry experts would agree that photogrammetry data compilation, though sounds easy, is quite a tedious task influenced by various external factors. The experience of IMP was no exception. Some of the challenges faced during the project life cycle and mitigation steps were:

1. Manpower mobilization- Kuwait has a small Photogrammetry industry in comparison to other third-world countries where there are many more photogrammetry production suppliers. Identifying experienced photogrammetry data compilers within the State of Kuwait posed to be a major challenge. The project could not be outsourced due to data sensitivity. In order to complete the task, manpower with experience in similar projects from the Middle East region were selected. With the onset of the COVID 19 pandemic, the selected manpower could not be mobilized on time due to the closure of international borders. In order to mitigate the risk of delay, locally available manpower was trained and used for data compilation. When International borders were open for foreigners to enter Kuwait, specialized manpower was mobilized
2. Changing the order of Survey- The project was conceptualized with photogrammetry data compilation as the first step, followed by land survey to update the attribute information. Since the photogrammetry data compilation schedule was pushed ahead, due to non-availability of manpower and other resources, the priority of areas of land survey had to be changed.
3. Updating Attribute information- Photogrammetrically compiled data does not have all the attribute information which are otherwise collected by field surveyors. Updating missing and/or incorrect attribute information to the compiled data was a challenge as some of the infrastructure had changed or were removed over time.
4. Connecting Above ground and Underground features- KOC's infrastructure such as pipelines, instrumentation cables, electric lines, etc., are both above and underground. Data compilation is possible for features visible and identifiable on stereo aerial images. However, underground assets can only be collected by field survey techniques. Working with data continuity from two sources is often a challenge. In order to overcome this, surveyors are provided with maps of areas where photogrammetry data compilation was completed. Changes to the above ground assets and connectivity of underground assets were updated.
5. Data currency- Aerial Images used for data compilation dates back to 2019, meaning the changes to the infrastructure post aerial acquisition date are not reflected in the images, making it difficult for surveyors to use the data in all areas. In order to overcome this, priority was given to areas within close vicinity of facilities such as Gathering Centers (GC) and Booster Stations (BS) where there would be little change to the infrastructure. Additionally, since the general topography within the oil fields have not changed much over the past three-years,

Photogrammetric Engineering & Remote Sensing
Vol. 89, No. 4, April 2023, pp. 197–201.
0099-1112/21/197–201

doi: 10.14358/PERS.89.4.197

the data was also used to generate a Digital Terrain Model (DTM).

Software

The selection of Software was another important step in the project's life cycle. KOC uses ESRI ArcGIS to create, edit, and store data. The ease of data integration within the enterprise GIS system could not be overlooked. Therefore, DATEM for ArcGIS and ArcGIS Pro software were selected for 3D visualization and data compilation. The selected software allows the user to edit, add, delete, and modify the features in the database concurrently. In addition, the data from feature compilation could be directly integrated to the enterprise GIS system.

Photogrammetry Data Compilation

The primary goal of the project was to update the digital database that users' access to manage the assets, analysis for modeling purposes, as well as produce hard-copy maps. In addition to KOC assets, to depict the terrain as per the required accuracy standards, breaklines are also being captured. Breaklines are compiled to support 1-meter contour interval. The data compilation is being carried out using digital photogrammetric vector data acquisition methods, skilled photogrammetry compilers, following strict quality control (QC) procedures. Data processing techniques, the algorithms used in the topographical structuring of the data, the processing sequence and the procedures employed in the production of the final dataset are in strict accordance with KOC specification.

The process involved in data compilation is shown in Figure 2:

- Input data consists of aerial images, exterior orientation (EO) parameters, camera details, etc. The number of images are checked against the corresponding EO file to ensure completeness.
- Project setup is completed in DATEM Summit Evolution and in ArcGIS Pro. The project setup in DATEM Summit Evolution is carried out by creating the camera file referring to ADS 30. A control file is created by importing the EO parameters obtained after the completion of the aerial triangulation process. The project is set to UTM Zone 38 N projection of WGS 84. In ArcGIS Pro, a new geodatabase is created followed by a mosaic dataset. Camera details are entered and the EO parameters from summit evolution are imported. Stereo models are built for data compilation.
- QC of the project setup involves verifying that the correct camera file is being used, checking if all the images are imported to the project, checking the stereo model footprint, checking the project parameters, etc.
- Data compilation is carried out adhering to KOC's specification and using the Enterprise Geodatabase. Tools within DATEM Summit Evolution such as contour generation and seamless update during data compilation come in handy during the production of the DTM. Only supplementary breaklines to support contours of 1-meter interval were compiled..

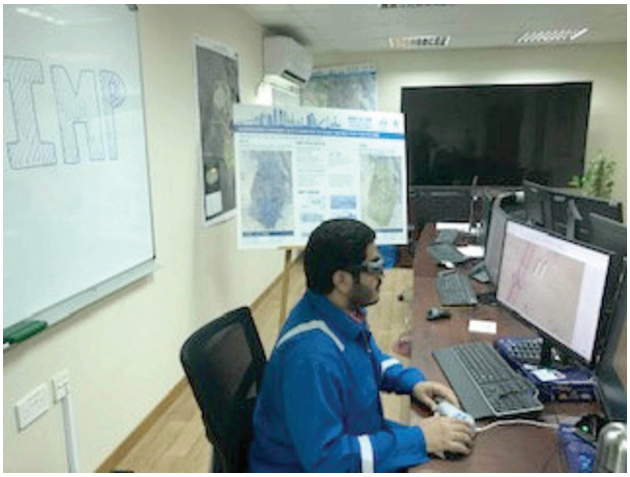

Figure 1. Photogrammetry Data Compilation.

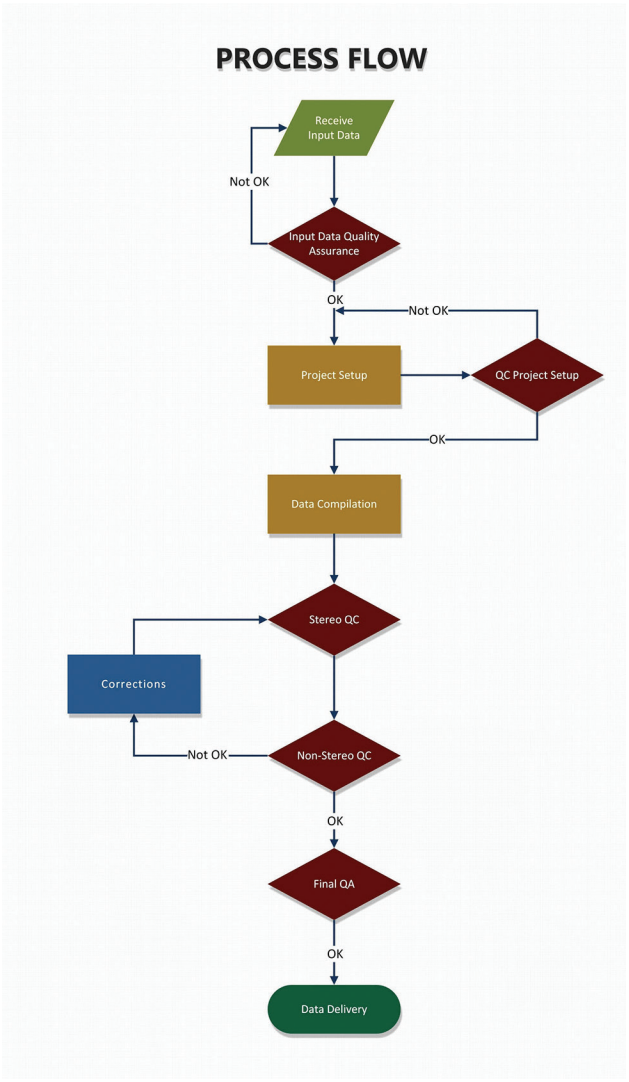

Figure 2. Process flow.

Stereo QC

- Stereo QC is performed on all compiled models for interpretation, omissions, and any other compilation errors.
- Checking the compiled data for positional and elevation accuracies.
- Checking the data for the correct usage of data structure/feature classes.
- Checking the edge match of the compiled model with adjacent models.
- Generating contours at 1-meter interval and checking for DTM quality.

Non-Stereo QC

- Verify model limits, buffer limits, and area limits to check completeness.
- Check for data connectivity and continuity between adjacent stereo models.
- Perform automated topological checks for overlaps, gaps, duplicates, etc., and perform corrections where required.
- Ensure uniform height in closed water polygons.

Metadata Creation

The Federal Geographic Data Committee's (FGDC) Content Standard for Digital Spatial Metadata (CSDGM) is a well-known metadata standard that is being used around the world. With ArcGIS 10, the metadata editor is capable of creating and publishing FGDC CSDGM metadata. Information such as Data Quality Information, Spatial Reference Information, Entity and Attribute Information, Distribution Information, Time Period Information, Contact Information, etc., are embedded into the metadata file.

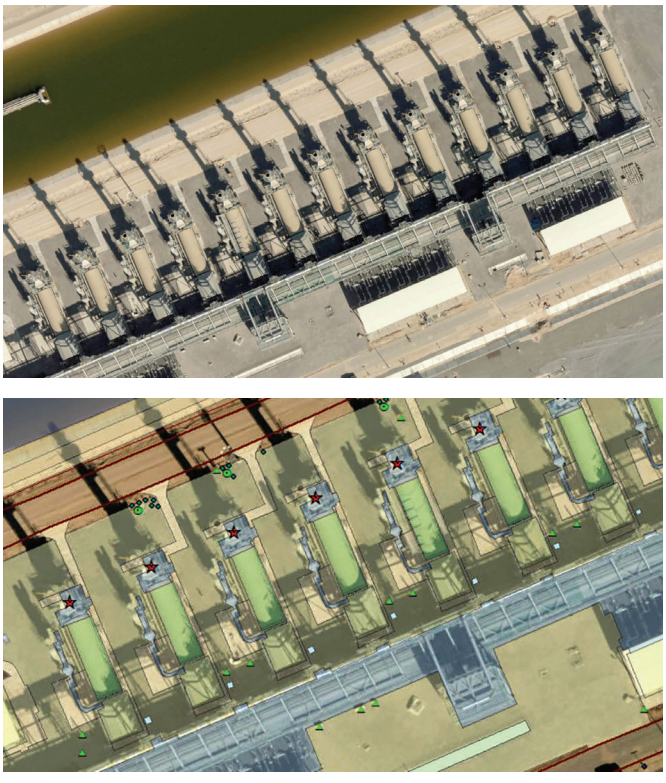

Figure 3. Hazardous area.

Advantages of Photogrammetric Data Compilation Over Land Survey

1. Data compilation in hazardous areas- The upstream process of oil and gas production in KOC involves several steps starting from exploration, extraction to production of crude oil and natural gas. One of the activities during production of crude oil is to burn gases that usually accompany oil. This process is called flaring. The area around smokestacks or flares have high level of toxic gases making it hazardous for the surveyors to be exposed to. However, this vital infrastructure must be mapped and the information included in the database. Mapping data through photogrammetry techniques allows this in a safer and faster way without having to physically visit areas with high levels of toxins. An illustration of one such area is shown in Figure 3.
2. Data compilation within inaccessible areas- The vital installations of KOC are often secured by a fence and require special permission for access. Also, these areas are not always accessible due to security reasons. Mapping assets within such installations through land survey techniques poses a challenge. In order to obtain information in these areas, photogrammetry techniques are used (See Figure 4).
3. Data collection in a faster way- Features such as pipelines over large areas would require surveyors to spend more time in the field collecting the data. Whereas, the same data, when collected photogrammetrically, saves a significant amount of time. To quantify the efforts, photogrammetry compilation takes about 30% of the time in comparison to field survey. The surveyors could use the vector data and update the attribute information thus saving several man-hours.
4. Creation of DTM- Compiling data photogrammetrically enhanced the creation of an accurate digital terrain model by delineating hard and soft breaklines; such as ridge lines, hilly areas, wadis, drains, hydrographic features, etc. The DTM thus created, is used to create contours on the fly and terrain information is updated in areas where the DTM does not accurately represent the ground.

Conclusion

Photogrammetry data compilation has helped KOC in optimizing their use of human resources to a great extent. In addition to mapping the KOC field assets faster, it also helps in keeping the working environment safe for the surveyors. This is done by mapping KOC assets photogrammetrically in hazardous and inaccessible areas, which would otherwise be not possible for the surveyors. It can be argued that the data compiled photogrammetrically would be less accurate in comparison with the field survey data. However, the purpose of this exercise was to fill in the missing information within hazardous and inaccessible areas which would be adequate for infrastructure planning purposes. The collected data was updated in the central enterprise geodatabase.

Data collected by field survey

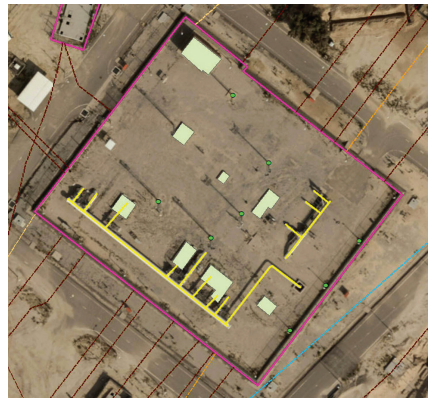

Additional data collected photogrammetrically

Dry Oil Lake

Figure 4. Inaccessible areas.

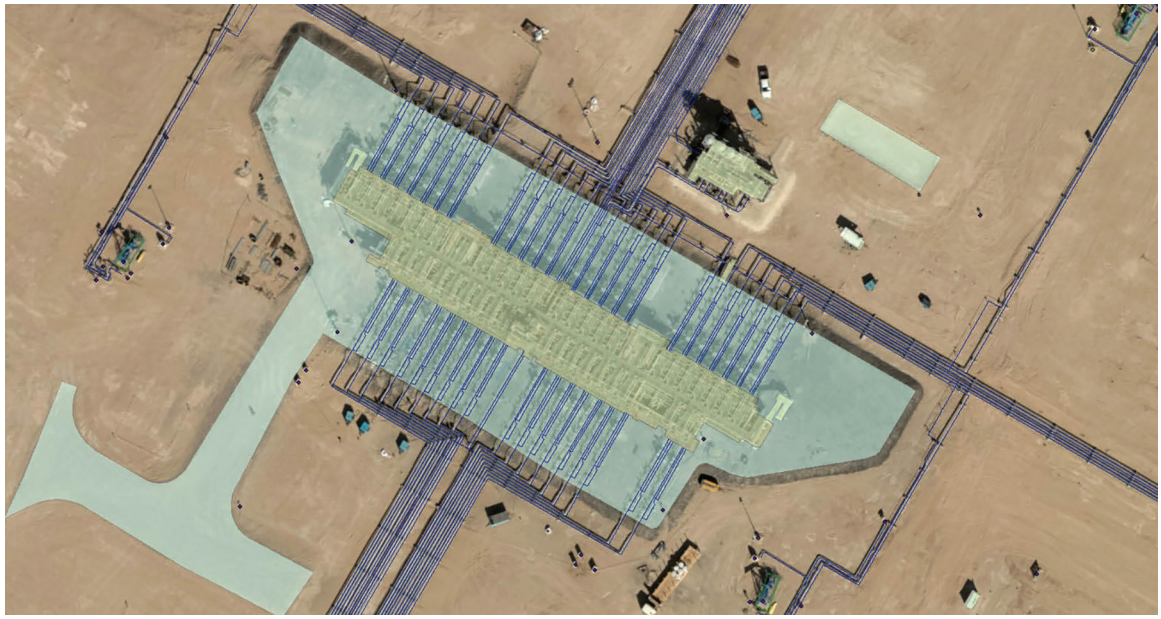

Figure 5. An example of pipelines over large areas.

PUBLISHING OPEN-ACCESS IN *PE&RS* IS NOW EASIER!

ASPRS is changing the subscription model of our monthly journal, *PE&RS*. ASPRS is waiving open-access fees for primary authors from subscribing institutions. Additionally, primary authors who are Individual Members of ASPRS will be able to publish one open-access article per year at no cost and will receive a 50% discount on open-access fees for additional articles.

- **Open Access matters!** By providing unrestricted access to research we can advance the geospatial industry and provide research that is available to everyone.
- **Institutions and authors receive more recognition!** Giving permission to everyone to read, share, reuse the research without asking for permission, as long as the author is credited.
- **Reputation matters!** Known for its high standards, *PE&RS* is the industry leading peer-review journal. Adding open access increases authors' visibility and reputation for quality research.
- **Fostering the geospatial industry!** Open access allows for sharing without restriction. Research is freely available to everyone without an embargo period.

Under the previous subscription model, authors and institutions paid $1500 or more in open-access fees per article. This will represent a significant cost savings. Open-access publications benefit authors through greater visibility of their work and conformance with open science mandates of funding agencies.

Subscriptions asprs.org/subscribe
Membership asprs.org/membership

asprs THE IMAGING & GEOSPATIAL INFORMATION SOCIETY

GIS Tips & Tricks

Al Karlin, Ph.D. CMS-L, GISP

Buffers Everywhere but Where You Want Them?

Here is yet another Tips & Tricks column that comes by way of my GIS/Map Making Class at the University of Tampa. About mid-way through the semester, after we have gone through discussion of map projections and coordinate systems, we start on introductory spatial analyses with the introduction of the "buffer". We construct buffers around points, lines, and polygons and use them to count objects within their limits.

In Figure 1, I started with some local hospitals (the blue "H"s) and Federal Qualified Health Centers (FQCHs: red crosses) in the Pittsburg, PA area (blue polygon). Then I constructed a 3-mile buffer (orange, semi-transparent ovals) around each hospital to analyze the number of FQCHs within 3 miles of the hospitals. The data originated from the US Census Bureau in geographic coordinates (not a projection system), so when I specified a 3-mile buffer radius, the buffers appear as ovals with the major axis along the latitude and the minor axis along the latitude, in North America. This confuses students to no end; the buffers should be circles not ovals!

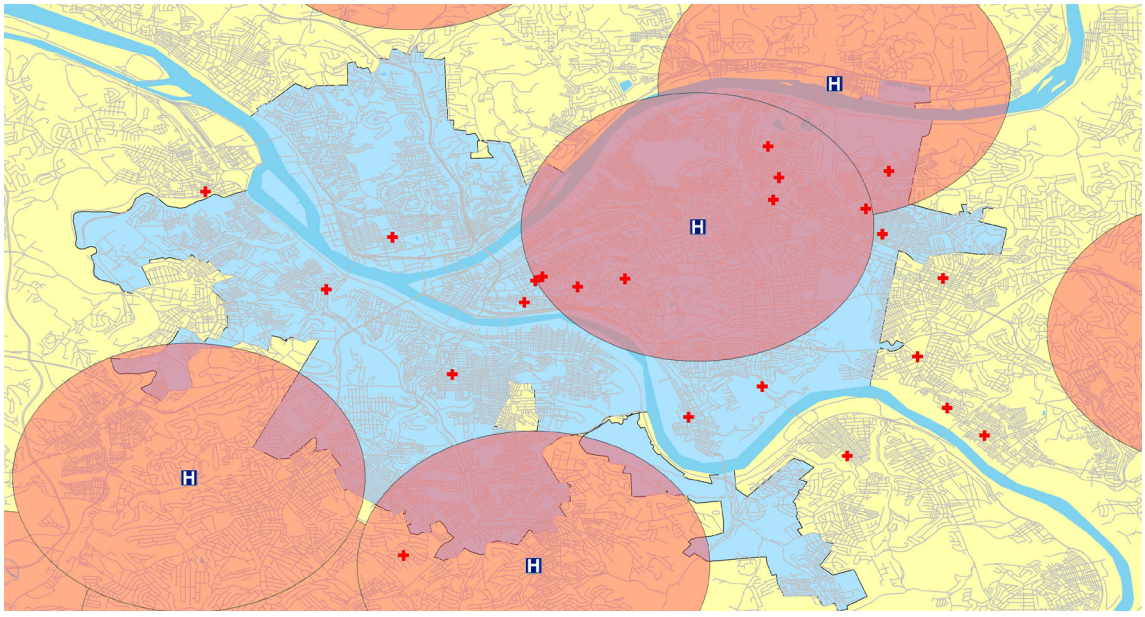

Figure 1. 3-mile Oval "buffers" around Hospitals resulting from the geographic coordinates (latitude/longitude) of the Hospital layer.

Creating buffers with any of the GIS software packages is easy; just find the tool (usually called, "Buffer"), identify the object to buffer, a buffer distance, set a few parameters (rounding, dissolved, etc.) and voila… a pretty instant spatial analysis. The buffer polygon can be used for spatial joins to count objects within, to select objects, and/or to clip other features. So, students gravitate to using and creating buffers for every analysis. However, in my classes, we generally start with some US Census Bureau data base map or some other layer that is in geographic coordinates, and therein lies the problem and this month's tip… Remember to change the coordinate system and projection before your make a buffer. The following example is from ArcGIS Pro 2.9, but the issues are similar with all GIS software programs.

There are a few different approaches to making "circular" buffers, but they all revolve around having the data in a projected coordinate system. Hence, my GIS class does not make buffers until they understand projections.

Photogrammetric Engineering & Remote Sensing
Vol. 89, No. 4, April 2023, pp. 203-204.
0099-1112/22/203-204

doi: 10.14358/PERS.89.4.203

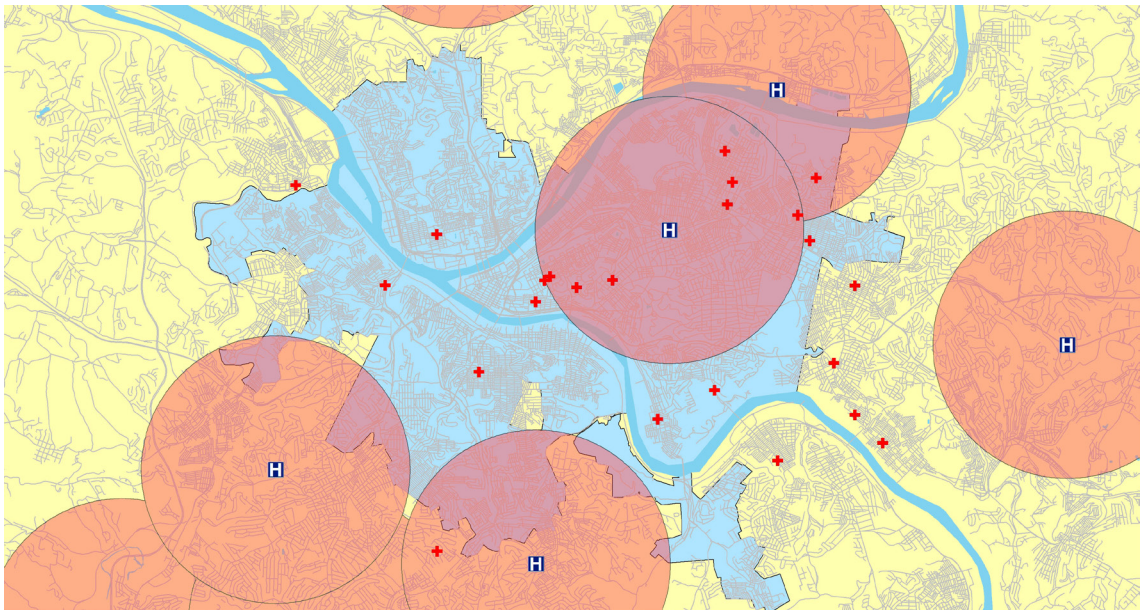

Figure 2. 3-mile circular "buffers" around Hospitals resulting from the projected coordinates (northings/eastings) of the Hospital layer.

Tip #1 — Project the source data BEFORE constructing the buffers. Most GIS software systems allow you to both specify a coordinate system (geographic or projected) for a data layer. In this case, the data layer should be defined as Geographic Coordinates with the North American Datum of 1983 (NAD83) or North American Datum of 1983 (2011). At most scales, the difference is negligible for our purposes. Then constructing the buffer using the appropriate geoprocessing tool will result in circular buffers as in Figure 2. In this case, I projected the geographic data into the Pennsylvania State Plane South (NAD 1983 (2011) FIPS 3702 (US Feet) coordinate system.

Tip #2 — Although not a preferred method, if you choose to maintain the DATA (point locations, buffers, etc.) in geographic coordinates, then you will get the same resulting map if you change the Data Frame coordinate system to the projected system. While the results will look the same, remember that distances may not be preserved by any on-the-fly projection calculations. So, for a "quick and dirty" map, just change the data frame coordinate system, but remember that the DATA are still in geographic coordinates.

Send your questions, comments, and tips to GISTT@ASPRS.org.

Al Karlin, Ph.D., CMS-L, GISP is with Dewberry's Geospatial and Technology Services group in Tampa, FL. As a senior geospatial scientist, Al works with all aspects of Lidar, remote sensing, photogrammetry, and GIS-related projects. He also teaches beginning map making at the University of Tampa.

Brian Huberty, *SharedGeo*

Great Lakes Remote Sensing: Binational, Petascale, Wetlands and Habitats Change Mapping

History

This Sector Insight article is based on international cooperation and shared geospatial data – all without a major exchange of international funding. This approach for sharing data and resources, across an international border, can be applied to almost any large area or complex monitoring program – as demonstrated here.

The seeds for this project were planted in the 1990's by the Great Lakes Information Network or GLIN (https://www.glc.org/glin). Roger Gauthier, with the Great Lakes Commission, led a series of Regional Data eXchange (RDX) Conferences with the goal of fostering the exchange of geospatial data between Canada and the US.

In 2010, the author was granted a Radarsat-2 data grant from the Canadian Space Agency SOAR Program to investigate the use of satellite imagery for wetland mapping in collaboration with the University of Minnesota. This grant also reignited a collaboration with Dr. Brian Brisco with the Canada Centre for Remote Sensing (CCRS). In 2015, I was sent to Ottawa to renew collaborations that grew out of the Great Lakes Information Network.

Significance

The Great Lakes make up about 84% of North America's freshwater surface area and about 21% of the world's freshwater surface area. The total surface area of the Great Lakes Basin is about 244,106 square kilometers (93,971 square miles), which is about 0.2% of the Earth's total surface area of about 510.1 million square kilometers (196.9 million square miles). In the future, when the freshwater Greenland and polar ice caps melt into the saltwater oceans, the 21% of the planet's freshwater surface area increases to about 50%. Thus making the Great Lakes System an important freshwater resource to monitor for future generations.

Wetlands are one of the most dynamic and significant landscape features which help store and filter freshwater flowing into the Great Lakes. Due to human and climate actions, Great Lakes citizens and government leaders are observing rapid change in both interior and coastal wetland habitats around the Great Lakes Basin. Government, business and academic stakeholders are asking for rapid, seasonal views of the basin where they can take direct action to fix these problems.

Satellite and aerial images are essential tools used to track and observe wetland and associated habitat changes over time for large areas like the Great Lakes Basin. These images can come from a variety of optical, RADAR, lidar and SONAR sensors which now require petascale computing to ingest and process derived products due to the frequency of collection and the higher resolution of the sensors.

Glars Project

Starting in 2016, the University of Minnesota, Michigan Tech University, Minnesota Department of Natural Resources, SharedGeo.org, the Canada Centre for Remote Sensing and Environment and Climate Change Canada joined forces to develop a set of complex wetland and surface water mapping products led by the U.S. Fish & Wildlife Service and funded by the Great Lakes Restoration Initiative. With significant Blue Waters supercomputer support from the National Science Foundation, MAXAR commercial satellite imagery was accessed and processed via the National Geospatial-intelligence Agency (NGA) NextView Program. The team was able to process and create a variety of remote sensing demonstration products across pilot areas as well as the entire Great Lakes Basin.

For example, all available, stereo, sub-meter, MAXAR optical satellite imagery for the Great Lakes Basin were processed to create 2-meter surface vegetation elevation models as depicted in Figure 1.

The optical stereo satellite imagery were also classified for a variety of wetland derived products over a dozen pilot sites as depicted in Figure 2.

Figure 2 shows the pre- and post-herbicide treatment of Phragmites Australis (an invasive plant), from 2016 to 2017 near Saginaw, Michigan, using high-resolution MAXAR satellite imagery. The lower right map derived from the 7/19/2017 satellite image shows a dark purple triangular shaped area in the upper left portion of the map that was

Photogrammetric Engineering & Remote Sensing
Vol. 89, No. 4, April 2023, pp. 205-207.
0099-1112/22/205-207

doi: 10.14358/PERS.89.4.205

Figure 1.

missed with herbicide treatment from the previous year. This example illustrates how land managers can be more accurate with treating wetlands to help eradicate an invasive plant.

Figure 3, taken between Michigan and Ontario, northeast of Detroit, of monthly Radarsat-2 images were collected and processed from 2016 through 2021. The objective was to show the dynamic water level rise over this six-year period as well as the duration of water saturation which is defined as a hydroperiod. A variety of fish and wildlife habitats are linked to these saturation zones.

Figure 2.

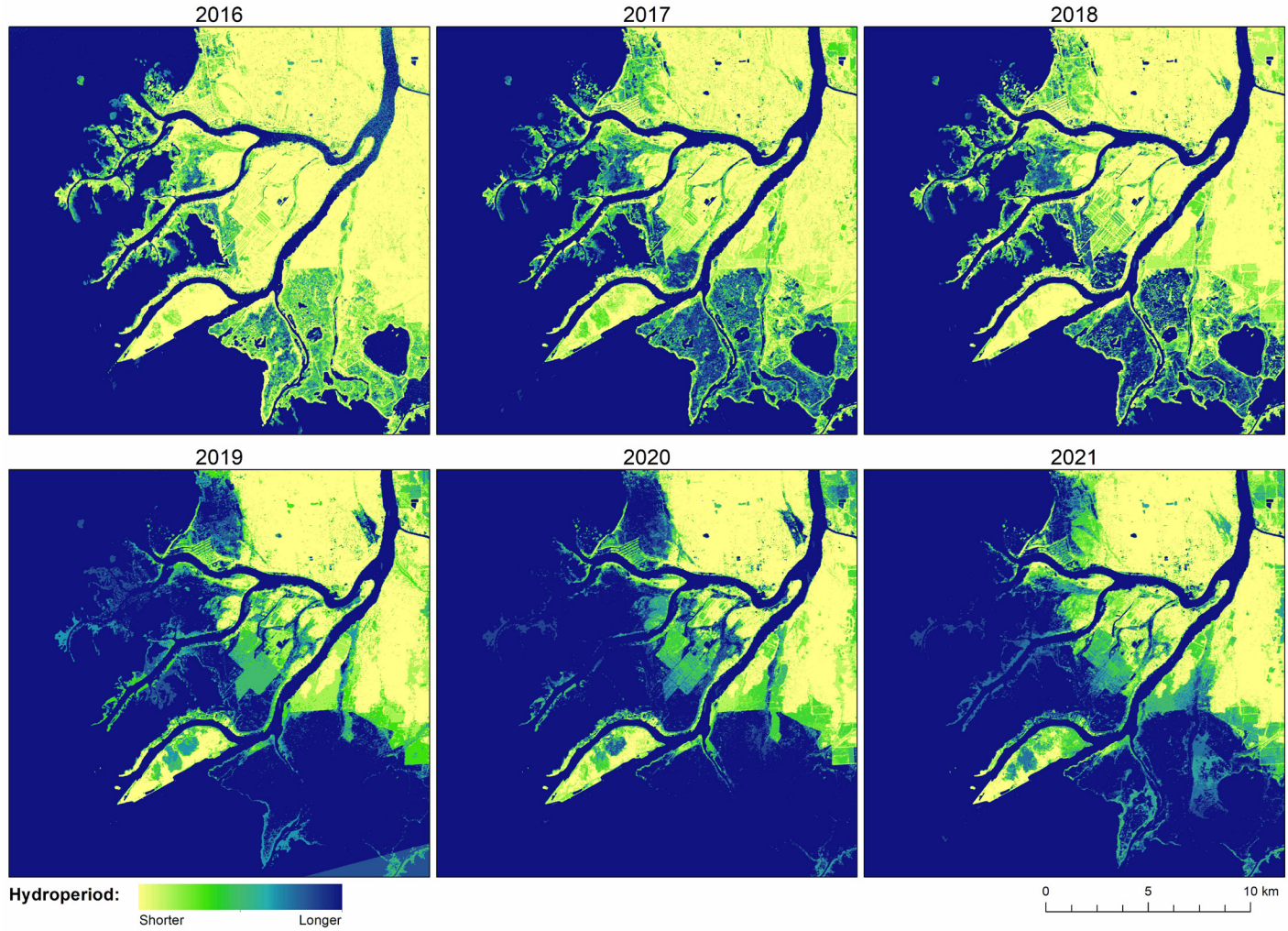

Figure 3.

What is the Future for Great Lakes Remote Sensing?

As a consequence of this project, the Great Lakes Alliance for Remote Sensing (GLARS) was formed to help further binational remote sensing of the Great Lakes and data distribution. The examples shown in this Sector Insight article can all be accessed at https://glars.org.

The Great Lakes Restoration Initiative funded this project to demonstrate the next generation tools from optical and radar imagery for submeter, high resolution, multi-temporal image products. The challenge for the future will be to develop this into a binational program to monitor and sustain the Great Lakes. Such an approach as this results in good, solid applications based on teamwork and cooperation rather than competition. Given the importance of the Great Lakes to Canada, the US, and the planet, it should be expected that this work will lead to an on-going, dedicated program.

Dedication

This column is dedicated to the late Dr. Brian Brisco, Canada Centre for Remote Sensing, Natural Resources Canada. Unfortunately, Brian passed away in September of 2022 after bravely battling illness for many years. Brian led the CCRS research and development for radar research and applications for surface and water features. His interest is not surprising since he was an avid muskie fisherman and duck hunter. Brian was the recipient of the Canadian Remote Sensing Society's Larry Morley Gold Medal Award in 2017.

Author

Brian Huberty is an ASPRS Certified Mapping Scientist who is currently assisting SharedGeo (a geospatial non-profit) with a variety of remote sensing projects. Over the last four decades, he has applied remote sensing and geospatial assessment technologies for the Minnesota Department of Natural Resources, USDA Forest Service, USDA Natural Resources Conservation Service, U.S. Geological Service and the U.S. Fish & Wildlife Service. Mr. Huberty has B.S. and M.S. degrees from the University of Minnesota, College of Natural Resources specializing in geospatial resource inventory systems. Brian has held leadership positions within ASPRS and ISPRS.

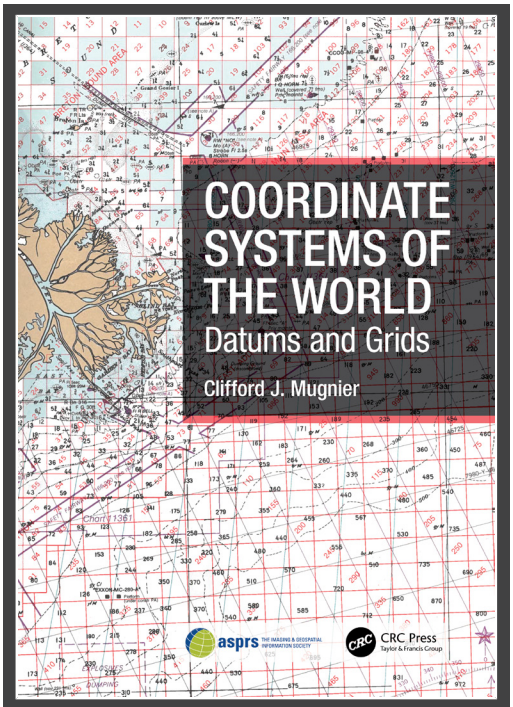

March 2023: 968pp
201 illustrations

Hb: 978-1-032-31034-3 | $220.00
eBook: 978-1-003-30778-5

TABLE OF CONTENTS:

Dedication; Foreword; Preface; Acknowledgement; List of Symbols used; Reference Ellipsoid; Afghanistan; Albania; Algeria; Andorra; Angola; Antigua/Barbuda; Argentina; Armenia; Aruba; Australia; Austria; Azerbaijan The Bahamas; Bahrain; Bangladesh; Barbados; Belarus; Belgium; Belize; Benin; Bhutan; Bolivia; Bosnia and Herzegovina; Botswana; Brazil; Brunei; Bulgaria; Burkina Faso; Burma; Burundi; Cambodia; Cameroon; Canada; Cape Verde; Cayman Islands; Central African Republic; Chad; Chile; China; Colombia; Comores; Democratic Republic of the Congo (Kinshasa); Republic of the Congo (Brassaville); Costa Rica; Croatia ; Cuba; Cyprus; Czechia; Denmark; Djibouti; Dominica; Dominican Republic; Ecuador; Egypt; El Salvador; Equatorial Guinea; Estonia; Ethiopia; Fiji; Finland; France; French Polynesia; Gabon; Gambia; Georgia; Germany; Ghana; Gibraltar; Greece; Grenada; Guadeloupe; Guam; Guatemala; Guinea; Guinea-Bissau; Guyana; Haïti; Honduras; Hong Kong; Hungary; Iceland; India; Indonesia; Iran; Iraq; Ireland; Israel; Italy; Ivory Coast; Jamaica; Japan; Jordan ; Kazakhstan; Kenya; Kiribati; Korea; Kuwait; Kyrgyzstan; Lao; Latvia; Lebanon; Lesotho; Liberia; Libya; Liechtenstein; Lithuania; Luxembourg; Macau; Macedonia; Madagascar; Malawi; Malaysia; Maldives; Mali; Malta; Marshall Islands; Martinique; Mauritania; Mauritius; Mexico; Micronesia; Moldova; Monaco; Mongolia; Montenegro; Montserrat; Morocco; Moçambique; Namibia; Nepal; Netherlands; New Zealand; Nicaragua; Niger; Nigeria; Niue; Norway; Oman; Pakistan; Panama; Papua New Guinea; Paraguay; Peru; Philippines; Poland; Portugal; Qatar; Romania; Russia; Rwanda; Sakhalin Island; Samoa Islands; Sao Tome e Principe ; Saudi Arabia; Senegal; Serbia; Seychelles; Sierra Leone; Singapore; Slovakia; Slovenia; Solomon Islands; Somalia; South Africa; Spain; Sri Lanka; St. Kitts and Nevis; St. Lucia; St. Vincent & Grenadines; Sudan; Suriname; Swaziland; Sweden; Switzerland; Syria; Taiwan; Tajikistan; Tanzania; Thailand; Timor-Leste; Togo; Tonga; Trinidad; Tunisia; Turkey; Turkmenistan; Tuvalu; Uganda; Ukraine; United Arab Emirates; United Kingdom; United States; Uruguay; Uzbekistan; Vanuatu; Venezuela; Vietnam; Yemen; Yugoslavia; Zambia; Zimbabwe.

20% Discount with Discount Code.

Coordinate Systems of the World

Datums and Grids

Clifford J. Mugnier

A comprehensive consolidation of data for the world, this book gives a short precis of each nation, each nation's history, its topography and a chronology of the development of geodetic surveying and coordinate systems for that specific nation. A starting point of information for understanding the world's datums and grids.

20% Discount Available - enter the code AFL01 at checkout*

Hb: 978-1-032-31034-3 | $176.00

** Please note that this discount code cannot be used in conjunction with any other offer or discount and only applies to books purchased directly via www.routledge.com. This code expires on 30 June 2023.*

For more details, or to request a copy for review, please contact: https://m.email.taylorandfrancis.com/review-copy-request-form

CRC Press
Taylor & Francis Group

Taylor & Francis Group
an **informa** business

For more information visit:
www.routledge.com/9781032310343

PE&RS' GRIDS & DATUMS COLUMN* IS NOW AVAILABLE AS A BOOK

Coordinate Systems of the World – Datums and Grids by Clifford J. Mugnier is a comprehensive consolidation of data based on the very popular Grids and Datums Column in *PE&RS*. This book provides a short precis of each country's history, topography, and a brief chronology of the development of their geodetic surveying and coordinate system.

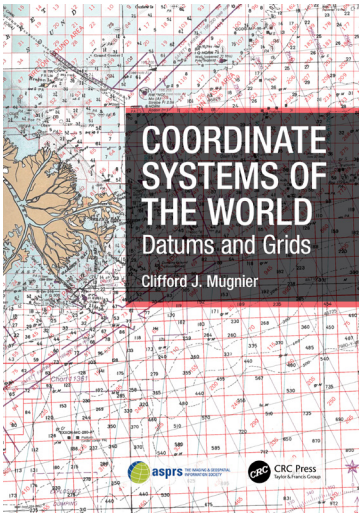

Coordinate Systems of the World – Datums and Grids was published by CRC Press, a Taylor & Frances Group and, for a limited time only is available at a discounted rate of $176. See page 208 for more information about this book and how to order.

*The contents of the Grids & Datums Column reflect the views of the author, who is responsible for the facts and accuracy of the data presented herein. The contents do not necessarily reflect the official views or policies of the American Society for Photogrammetry and Remote Sensing and/or the Louisiana State University Center for GeoInformatics (C^4G).

NEW ASPRS MEMBERS

ASPRS would like to welcome the following new members!

Ossai David Alu
John P. Cannon Jr
Belinda Damewood
Michael Dauer
Javier De La Rocha
Michael Ewing
Elaina Gonsoroski
Travis Howell
Teodoro De Jesús Jiménez Durán
Paul Kokes
Jonathan Lee
John Milburn
Scott Myatt
Cole Allen Perry
Lauren Pfund
Edward Rantanen
Laure Lung Reed
Amanda Roberts
Ashish GS Srinivasan
Randy K. Voorhees, II

FOR MORE INFORMATION ON ASPRS MEMBERSHIP, VISIT
HTTP://WWW.ASPRS.ORG/JOIN-NOW

ASPRS' MAY GEOBYTE IS SCHEDULED FOR MAY 5TH

SeaSketch 2.0: A New, Free and Open-source Software Service for Map-based Surveys and Collaborative Geodesign

May 5th at 12 Noon ET

Originally launched in 2012, SeaSketch (www.seasketch.org) was developed to support the collaborative geodesign of marine spatial plans. Users can visualize dynamic maps, contribute information by way of map-based surveys, sketch and evaluate prospective zones (such as marine protected areas), and share designs in interactive forums. The new version of SeaSketch, available in the first quarter of 2023, substantially benefits users through new and improved functionality including (1) mobile / table compatibility, (2) vector-based map rendering to improve performance, (3) capabilities for working offline, (4) data hosting, (5) built-in cartographic tools and (6) an entirely free and open-source code base. I will demonstrate the core user-facing and administrative tools, drawing from a number of ongoing participatory mapping projects using SeaSketch on a national scale. Attendees will learn the basics for creating their own bespoke SeaSketch projects.

Presented by Will McClintock, Ph.D., Will McClintock is a marine scientist at the National Center for Ecological Analysis and Synthesis (NCEAS) within the University of California Santa Barbara (UCSB). He has over 20 years of experience developing and implementing software tools for marine spatial planning (MSP), conservation and fisheries management. As a member of the Blue Prosperity Coalition, he is currently supporting MSP in The Maldives, The Azores, Bermuda, Samoa, Fiji and other geographies. Other past and ongoing project locations include the US, UK, Canada, New Zealand, Norway, The Cook Islands, Gyana, Reunion, Indonesia and Australia. He received a B.A. in Biology from Earlham College, M.S. in Behavioral Ecology from the University of Cincinnati, M.A. in Counseling Psychology from Pacifica Graduate Institute, and a Ph.D. in Ecology, Evolution and Marine Biology from UCSB.

All live GeoBytes are complimentary to everyone—Register at www.asprs.org/geobytes.html

ASPRS Staff Directory

Membership/*PE&RS* Subscription/ Conferences
Yuki Day
office@asprs.org

Advertising/Exhibit Sales
Bill Spilman
bill@innovativemediasolutions.com

Peer-Review Article Submission
Alper Yilmaz
PERSeditor@asprs.org

Highlight Article Submission
Jie Shan
jshan@ecn.purdue.edu

Feature Article Submission
Featureeditor@asprs.org

Certification
applications@asprs.org

Calendar
calendar@asprs.org

ASPRS Bookstore
office@asprs.org

ASPRS Foundation
foundation@asprs.org

Mailing Address
PO Box 14713
Baton Rouge, LA 70898
301-493-0290, 225-408-4422 (fax)
www.asprs.org

ASPRS Workshop Series

It's not too late to earn Professional Development Hours

Miss one of our Live Online Workshops? You can purchase the workshops now and watch when you are ready!

Check out the workshops offered by visiting **https://asprs.prolearn.io/catalog**

A GPU-Accelerated PCG Method for the Block Adjustment of Large-Scale High-Resolution Optical Satellite Imagery Without GCPs

Qing Fu, Xiaohua Tong, Shijie Liu, Zhen Ye, Yanmin Jin, Hanyu Wang, and Zhonghua Hong

Abstract

The precise geo-positioning of high-resolution satellite imagery (HRSI) without ground control points (GCPs) is an important and fundamental step in global mapping, three-dimensional modeling, and so on. In this paper, to improve the efficiency of large-scale bundle adjustment (BA), we propose a combined Preconditioned Conjugate Gradient (PCG) and Graphic Processing Unit (GPU) parallel computing approach for the BA of large-scale HRSI without GCPs. The proposed approach consists of three main components: 1) construction of a BA model without GCPs; 2) reduction of memory consumption using the Compressed Sparse Row sparse matrix format; and 3) improvement of the computational efficiency by the use of the combined PCG and GPU parallel computing method. The experimental results showed that the proposed method: 1) consumes less memory consumption compared to the conventional full matrix format method; 2) demonstrates higher computational efficiency than the single-core, Ceres-solver and multi-core central processing unit computing methods, with 9.48, 6.82, and 3.05 times faster than the above three methods, respectively; 3) obtains comparable BA accuracy with the above three methods, with image residuals of about 0.9 pixels; and 4) is superior to the parallel bundle adjustment method in the reprojection error.

Introduction

A large number of high-resolution optical satellites have been launched in the world and in China, such as SPOT-5 (Poli, Zhang, and Gruen 2004), IKONOS (Toutin and Cheng 2000), QuickBird (Noguchi *et al.* 2004), GeoEye (Fraser and Ravanbakhsh 2009), and Ziyuan-3 (ZY-3) (Tang *et al.* 2013; Jiang *et al.* 2015; Liu *et al.* 2016; Tong *et al.* 2015a; Tong *et al.* 2015b; Gong *et al.* 2017; Yang *et al.* 2017), which is China's first civil stereo surveying and mapping satellite. The ground resolution and geo-positioning accuracy of these systems are constantly being improved. The precise geo-positioning of high-resolution optical satellite imagery (HRSI) without ground control points (GCPs) is the premise for large-scale remote sensing mapping applications, including global mapping (Gong *et al.* 2017), three-dimensional modeling (Yang *et al.* 2017), and so on. However, there are two critical issues in large-scale block adjustment (BA) without GCPs: 1) how to improve the accuracy (Zhang *et al.* 2016; Chen *et al.* 2016; Wang *et al.* 2017; Ma *et al.* 2017; Jiao *et al.* 2018; Cao *et al.* 2019) of BA without GCPs; and 2) how to improve the calculation efficiency (Zhang *et al.* 2014; Zheng *et al.* 2016; Gong *et al.* 2017; Yang *et al.* 2017; Wang *et al.* 2017; Sun *et al.* 2019) of large-scale BA.

The main HRSI systems, such as SPOT-5, IKONOS, and QuickBird, do not have a high accuracy of direct positioning (Zhang *et al.* 2016; Gong *et al.* 2017; Wang *et al.* 2017). The Rational Polynomial Coefficient (RPC) parameters contain obvious systematic errors, so that it is necessary to establish a corresponding error compensation model (Tao and Hu 2001; Fraser and Hanley 2005). Grodecki and Dial (2003) analyzed the systematic error of the RPC model and used an affine transformation model to correct the systematic errors; Zhang *et al.* (2016) improved the BA accuracy of SPOT-5 satellite images from 13.7 m to 5 m in the planar, and from 9 m to less than 5 m in the elevation; and Tong, Liu, and Weng (2009) studied a method of RPC systematic error correction and RPC parameter refinement and regeneration and assessed the accuracy of QuickBird satellite stereo images (Tong *et al.* 2010). In order to improve the BA accuracy of HRSI without GCPs, researchers have carried out a series of related studies. Yao *et al.* (2018) adopted a BA method based on repeated satellite images covering the same area, which improved the BA accuracy without GCPs. In addition, Pan *et al.* (2017) achieved better BA results by using other satellite image or aerial image with a higher geo-positioning accuracy as control information. Moreover, the geocoded information data, such as digital orthophoto models and digital elevation models (DEMs), can also be used as control data for the combined BA of satellite images (Zhang *et al.* 2016). For example, Zhou *et al.* (2018) used Shuttle Radar Topography Mission data to interpolate the elevation values of ground points corresponding to tie points as the initial adjustment values, which improved the BA accuracy, especially in the elevation direction. In addition, multi-source control information, such as synthetic aperture radar imagery (Zhang *et al.* 2021), high-precision optical satellite imagery (Pan *et al.* 2017), high geo-positioning aerial images (Song *et al.* 2021), or laser altimetry data (Jiao *et al.* 2018; Zhang *et al.* 2021) can also be introduced to carry out combined BA. Another approach is to use an independent model method (Chen *et al.* 2016), minimum height difference method (Chen *et al.* 2016), or other methods to match a certain number of virtual control points between the original images and the public geographic information data to improve the BA accuracy without GCPs (Zhang *et al.* 2016; Chen *et al.* 2016; Tong *et al.* 2020).

Due to the large number of images in large-scale BA and the complex structure of BA networks, large-scale BA without GCPs needs further study in practical applications. For large-scale BA, scholars have carried out some related research, including optimizing the minimum bandwidth to reduce the memory consumption of the normal equation (Wang *et al.* 2017). Although there are some effective computing methods for matrix decomposition, the inversion of large matrices (Agullo *et al.* 2011), the memory consumption of the normal equation, and the BA computing efficiency are all issues that need to be solved. Among the different methods, Zheng *et al.* (2016) proposed

Qing Fu, Xiaohua Tong, Shijie Liu, Zhen Ye, Yanmin Jin, Hanyu Wang, and Zhonghua Hong are with the College of Surveying and Geo-informatics, Tongji University, Shanghai 200092, China (xhtong@tongji.edu.cn).

Qing Fu is also with the School of Electronics and Information Engineering, Jinggangshan University, Ji'an 343009, China.

Zhonghua Hong is also with the College of Information Technology, Shanghai Ocean University, Shanghai, 201306, China.

Contributed by Rongjun Qin, February 14, 2022 (sent for review June 1, 2022; reviewed by San Jiang, Xiao Ling, Mostafa Elhashash).

Photogrammetric Engineering & Remote Sensing
Vol. 89, No. 4, April 2023, pp. 211–220.
0099-1112/22/211–220

doi: 10.14358/PERS.22-00051R2

a method based on DEM-assisted BA to improve the mapping accuracy for large numbers of images, and they carried out a BA experiment using ZY-3 and GF-1 images covering Jiangxi province of China. D'Angelo and Reinartz (2012) presented rational function model (RFM) to improve the BA accuracy of 414 pairs of CartoSat-1 stereo images covering northern Italy; Zhang *et al.* (2014) used the rigorous imaging geometry model to carry out a BA experiment without GCPs for ZY-3 three-line array (TLA) stereo images with a maximum length of 3000 km, in which, compared with the geo-positioning accuracy of forward intersection, the BA accuracy without GCPs for the ZY-3 satellite was greatly improved, reaching a planar accuracy of 8.3 m and an elevation accuracy of 5.0 m; Wang *et al.* (2017) used a conjugate gradient (CG) method to estimate the BA results, and a BA experiment without GCPs for 8802 ZY-3 TLA stereo images covering the whole of mainland China was carried out, which needed only two iterations to converge and cost about 15 min on a standard computer for the BA estimation (Gong *et al.* 2017; Yang *et al.* 2017); and Sun *et al.* (2019) proposed a multi-threaded parallel computing method based on RFM, which uses the OpenMP parallel computing method, and the time cost of the BA estimation was less than 7.5 min for the experimental area covered by 5241 ZY-3 satellite images. However, BA model estimation is still a time-consuming task in HRSI without GCPs, especially in the large scale. Furthermore, relatively few studies have combined the Preconditioned Conjugate Gradient (PCG) and Graphic Processing Unit (GPU) parallel computing methods for the large-scale BA of HRSI without GCPs.

In recent years, with the development of high-performance parallel GPU computing devices, the application of GPUs has not been confined to the field of the graphics display. Many CPU computing tasks can also be accomplished with parallel GPU computing devices, and GPUs can provide a computing performance that is tens or even hundreds of times faster than that of a CPU in the Single Instruction Multiple Data operations. As a result, GPU devices have been widely used in the field of high-performance computing for non-graphical displays. Before this, there had been lots of research work on BA using GPU devices in the computer vision community (Agarwal *et al.* 2010; Choudhary, Gupta, and Narayanan 2010; Wu *et al.* 2011; Liu, Gao, and Hu 2012; Hänsch, Drude, and Hellwich 2016; Zheng *et al.* 2017), which mainly focused on close-range photogrammetric digital images and unmanned aerial vehicle images. Zheng *et al.* (2017) used a combined PCG and GPU computing method for the BA of a data set with about 4500 digital images from the Community Photo Collections (CPC) project, where nine million image points could be processed in only 1.5 minutes while achieving a subpixel accuracy. Combining PCG and a high-performance GPU parallel computing method for the large-scale BA of HRSI without GCPs faces with three main problems: 1) estimation of the BA based on the PCG method; 2) the memory consumption of the error equation based on the Compressed Sparse Row (CSR) (Nathan and Garland 2009) sparse matrix format; and 3) the GPU-accelerated PCG method for BA estimation.

Therefore, in this paper, we present a combined PCG and GPU parallel computing method for the large-scale BA of HRSI without GCPs. In the proposed approach, the PCG method is used to calculate the unknown parameter results after BA model construction, which avoids the direct inversion of the design matrix of the normal equation. In addition, the CSR sparse matrix format is used to reduce the memory consumption of the normal equation, especially for large-scale BA experiments, and the combined PCG and GPU parallel computing method is used to further improve the computational efficiency of the BA model.

Methodology

Figure 1 shows the overall technical flowchart of the proposed BA method, i.e., the combined PCG and GPU parallel computing method for the large-scale BA of HRSI without GCPs, which consists of three main components, as follows:

(1) Construction of the BA model based on RFM, which is the premise of large-scale BA estimation for HRSI without GCPs.
(2) The PCG method is used to calculate the normal equation, the CSR sparse matrix format is used to save the memory consumption, and to accelerate the matrix operations of the correlation coefficients.
(3) The combined PCG and GPU parallel computing method is adopted to improve the efficiency of the whole BA estimation process.

Construction of the BA Model Based on RFM Without GCPs

The Rational Function Model

The imaging geometric model represents the geometric physical relationship between the image point coordinates and the ground point coordinates, which is the prime of the high-precision geo-positioning of remote sensing images. RFM is a more general expression of the sensor model and is suitable for all kinds of sensors (Tong *et al.* 2010; Chen *et al.* 2016; Zhang *et al.* 2016; Gong *et al.* 2017; Yang *et al.* 2017). From a numerical calculation point of view, RFM can be understood as a functional relationship, with the ground point coordinates as the independent variables and the image point coordinates as the dependent variables. The basic form is shown in Equation 1 (Tao and Hu 2001; Grodecki and Dial 2003; Fraser and Hanley 2005):

$$\begin{cases} r_n = \dfrac{\mathrm{Num}_L\left(P_n, L_n, H_n\right)}{\mathrm{Den}_L\left(P_n, L_n, H_n\right)} \\ c_n = \dfrac{\mathrm{Num}_L\left(P_n, L_n, H_n\right)}{\mathrm{Den}_L\left(P_n, L_n, H_n\right)} \end{cases} \tag{1}$$

where the dependent variable (r, c) represents the normalized image point coordinates in the scan direction and flight direction, and the independent variable (P, L, H) represents the normalized ground point coordinates. Num_L, Den_L, Num_S, and Den_S are general polynomials for different combinations of (P, L, H). In a polynomial, the power of each independent variable is no more than three, and the sum of the independent variables' power is also no more than three (Tao and Hu 2001; Grodecki and Dial 2003). Therefore, each polynomial is the sum of 20 different combinations of independent variables. The coefficients of the four polynomials and the normalized coefficients constitute the RFM coefficients (RPC) (Fraser and Hanley 2005; Tong *et al.* 2010).

Normalizing can improve the stability of solving the RFM coefficients and is used to reduce the data rounding errors caused by the large difference of the data series in the calculation procedure (Tong *et al.* 2010; Zhang *et al.* 2016; Gong *et al.* 2017; Yang *et al.* 2017). Normalizing is achieved by a translation and scaling procedure. The normalized equation is shown in Equation 2 (Tao and Hu 2001; Grodecki and Dial 2003; Fraser and Hanley 2005):

$$\begin{gathered} r_n = \frac{r - r_0}{r_s}, c_n = \frac{c - c_0}{c_s} \\ P_n = \frac{P - P_0}{P_s}, L_n = \frac{L - L_0}{L_s}, H_n = \frac{H - H_0}{H_s} \end{gathered} \tag{2}$$

where r_0, c_0, P_0, L_0, H_0 are the normalized translation parameters, and r_s, c_s, P_s, L_s, H_s are the normalized scaling coefficients.

Construction of the BA Model Without GCPs

The systematic errors of the RFM are corrected by the additional compensation model in the image space (Tong *et al.* 2010; Zhang *et al.* 2016; Gong *et al.* 2017; Yang *et al.* 2017). Equation 1 can then be rewritten as:

$$\begin{cases} r + \Delta r = \dfrac{Num_L\left(P, L, H\right)}{Den_L\left(P, L, H\right)} \\ c + \Delta c = \dfrac{Num_s\left(P, L, H\right)}{Den_s\left(P, L, H\right)} \end{cases} \tag{3a}$$

$$\begin{cases} \Delta r = a_0 + a_1 r + a_2 c \\ \Delta c = b_0 + b_1 r + b_2 c \end{cases} \tag{3b}$$

where Δr, Δc are the systematic error correction parameters of the optical satellite imagery in the scan and flight directions, respectively; and $(a_0, a_1, a_2, b_0, b_1, b_2)$ are the compensation parameters of the systematic

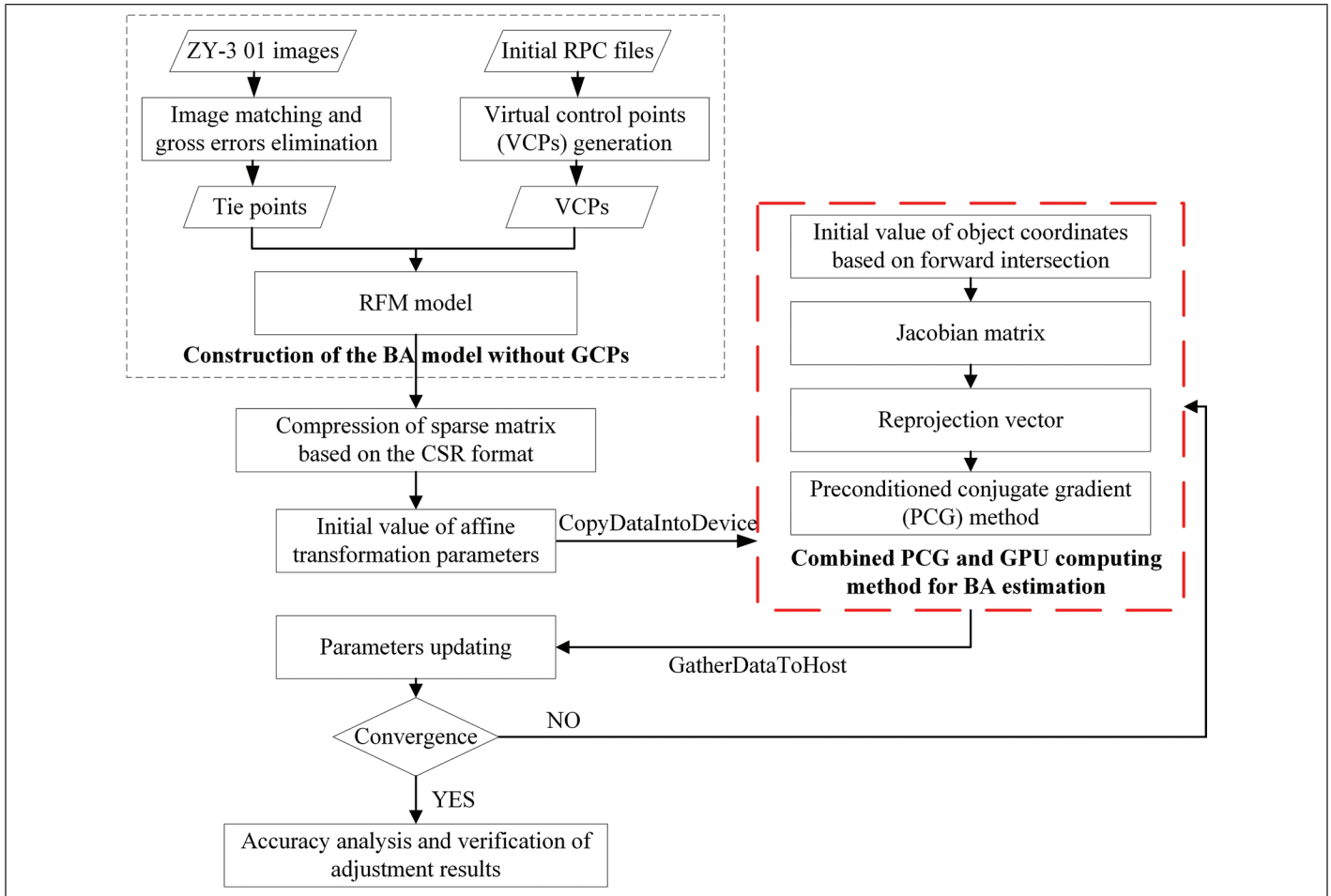

Figure 1. Flowchart of the proposed block adjustment (BA) method. (The red box represents the calculation process in Graphic Processing Unit (GPU) device).

errors. a_0 and b_0 are mainly used to compensate the system offset errors caused by model drift. a_1 and b_1 can be approximated to eliminate the model scanning direction errors caused by roll attitude. a_2 and b_2 can be used to eliminate the flight direction errors caused by pitch attitude (Tao and Hu 2001; Grodecki and Dial 2003). Due to the imaging characteristics of satellite platforms, the attitude compensation values are usually small (Fraser and Hanley 2005; Tong *et al.* 2010).

Equation 3a can be linearized by Taylor series expansion (Grodecki and Dial 2003), the matrix form is as follows:

$$\mathbf{V} = \mathbf{At} + \mathbf{Bx} - \mathbf{L}, \mathbf{P} \tag{4}$$

where $\mathbf{V}$ represents the residual error vectors of the tie point measurements in the scan and flight directions; $\mathbf{A}$, $\mathbf{B}$ are the corresponding coefficient matrices; $\mathbf{x}$ represents the correction vectors of the ground point coordinates corresponding to the tie points; $\mathbf{t}$ represents the correction vectors of the systematic error; $\mathbf{L}$ is the constant vector calculated from the initial value; and $\mathbf{P}$ represents the corresponding weight matrices.

According to the theory of least squares, the observed error equation can be further modified. Equation 4 can then be written as:

$$\begin{bmatrix} \mathbf{A}^T\mathbf{PA} & \mathbf{A}^T\mathbf{PB} \\ \mathbf{B}^T\mathbf{PA} & \mathbf{B}^T\mathbf{PB} \end{bmatrix} \begin{bmatrix} \mathbf{t} \\ \mathbf{x} \end{bmatrix} = \begin{bmatrix} \mathbf{A}^T\mathbf{PL} \\ \mathbf{B}^T\mathbf{PL} \end{bmatrix} \tag{5}$$

The normal equation matrix described in Equation 5 is a symmetric banded matrix. Therefore, in the BA estimation procedure, because there are too many unknowns, it is necessary to separate the affine transformation coefficients from the coordinate corrections of the ground points. In other words, we first eliminate a class of unknowns (generally the coordinate corrections of ground point $\mathbf{x}$ (Gong *et al.* 2017; Yang *et al.* 2017)), and we obtain the modified normal equation containing only the parameters of the affine transformation coefficients $\mathbf{t}$. After eliminating $\mathbf{x}$, the solution of $\mathbf{t}$ can be shown as:

$$\mathbf{N}_t \times \mathbf{t} = \mathbf{R}_t \tag{6}$$

where $\mathbf{N}_t = \mathbf{A}^T\mathbf{PA} - \mathbf{A}^T\mathbf{PB} \times (\mathbf{B}^T\mathbf{PB})^{-1} \times \mathbf{B}^T\mathbf{PA}$ is the Schur complement matrix, which is a symmetric matrix, $\mathbf{N}_t = \mathbf{A}^T\mathbf{PL} - \mathbf{A}^T\mathbf{PB} \times (\mathbf{B}^T\mathbf{PB})^{-1} \times \mathbf{B}^T\mathbf{PL}$.

After calculating the corrections of the affine transformation parameters of each image, according to the calculation results of the modified normal equation, the corrections of the ground point coordinates $\mathbf{x}$ corresponding to the tie points are solved by replacing the normal Equation 5, and then the solution of $\mathbf{x}$ can be shown as:

$$\mathbf{x} = (\mathbf{B}^T\mathbf{PB})^{-1} \times (\mathbf{B}^T\mathbf{PL} - \mathbf{B}^T\mathbf{PA} \times \mathbf{t}) \tag{7}$$

The BA solution is an iterative procedure. When the results of two BA solutions are less than the set threshold, the iterative procedure is stopped (Chen *et al.* 2016; Gong *et al.* 2017; Yang *et al.* 2017; Tong *et al.* 2020).

In addition, the virtual control points are generated from the initial RPC files in a regular grid (Yang *et al.* 2017).

Estimation of the Modified Normal Equation Based on Sparse Matrix and PCG Method

Storage and Compression of the Sparse Coefficient Matrix

The coefficient matrix of the normal equation in the large-scale BA model has obvious sparsity. For the large-scale sparse matrix, if a full-matrix

storage format is used to store the dense matrix, its storage requirement and computational time cost will be very high, and it will cost lots of unnecessary memory space. If a compressed storage format method is used to store the sparse coefficient matrix, it will not only reduce memory consumption, but will also reduce the computational time cost.

The common storage formats for sparse matrices include Coordinate (COO), Compressed Sparse Column, and Compressed Sparse Row (CSR) (Nathan and Garland 2009; Cheng, Tian, and Ma 2018). The COO format stores a sparse matrix by using the three arrays of values, rows, and columns index (colind), as shown in Figure 2a. CSR uses the three arrays of values, rows pointer (rowptr), and colind to store a sparse matrix, as shown in Figure 2b, which is suitable for the coefficient matrix storage and parallel matrix computing. At the same time, the value can be obtained from the row's pointer and columns index in the GPU device, respectively, then the sparse design matrix stored in the CSR format can better meet the characteristics of GPU parallel computing. In this study, we used the CSR storage format to compress the sparse design matrix of the modified normal equation.

Estimation of the Modified Normal Equation Based on the PCG Method

The CG method can make full use of the sparsity of the normal matrix and can be calculated without pre-estimating other parameters. In addition, the calculation required in each iteration is mainly the operation between vectors, which is convenient and easy for parallelization. The convergence speed of the CG method is closely related to the condition number of the design matrix (Zheng *et al.* 2017). The CG method can obtain high-precision approximate calculation results in fewer iterations. However, when the condition number of the design matrix is very large, the convergence speed is very slow. In the preconditioned conjugate gradient (PCG) method, after introducing the preconditioner matrix $\mathbf{M}$ through an appropriate preconditioning method, the eigenvalue distribution of the matrix is more centralized and the condition number of the design matrix is greatly reduced, so as to further improve the convergence speed. The PCG method is a very effective and efficient iterative method for solving large-scale sparse linear equations (Peng, Liu, and Wei 2021).

There are many preconditioning methods for symmetric positive definite linear equations, such as the diagonal preconditioner matrix (Wathen and Silvester 1993), the Jacobi preconditioning method (Byröd and Åström 2010), incomplete matrix decomposition (Bru and Tůma 2008), the multi-scale preconditioning matrix (Byröd and Åström 2009), etc. However, there is no general method that can be used to all the computational problems in which the condition number of the sparse design matrix is obviously different. The PCG method does not need to decompose the coefficient matrix, which can effectively reduce the memory consumption and improve the computational efficiency. The block Jacobi preconditioning matrix (Wu *et al.* 2011) is very simple, easy to calculate, and the preconditioned matrix is very stable, which satisfies the selection principle of the preconditioned matrix. Therefore, in this study, the block Jacobi preconditioning matrix was used to estimate the normal equation for the large-scale BA.

In Equation 6, $\mathbf{N}_t$ is an n-order positive definite symmetric matrix, and $\mathbf{t}$ and $\mathbf{R}_t$ are n-dimensional column vectors. If $\mathbf{M}$ is a preconditioner matrix, the PCG method is listed in Algorithm 1.

Algorithm 1: The preconditioned conjugate gradient (PCG) method

For $k = 0$;
Initial parameters: $\mathbf{t}^{(0)} = 0$, $\mathbf{r}^{(0)} = \mathbf{R}_t - \mathbf{N}_t\mathbf{t}^{(0)}$, $\mathbf{d}^{(0)} = \mathbf{M}^{-1}\mathbf{t}^{(0)}$

do
1: $\alpha^{(k)} = \mathbf{r}_k^{\mathrm{T}}\mathbf{M}^{-1}\mathbf{r}^{(k)}/\mathbf{d}_k^{\mathrm{T}}\mathbf{N}_t\mathbf{d}^{(k)}$
2: $\mathbf{t}^{(k+1)} = \mathbf{t}^{(k)} + \alpha^{(k)}\mathbf{d}^{(k)}$
3: $\mathbf{r}^{(k+1)} = \mathbf{t}^{(k)} + \alpha^{(k)}\mathbf{d}^{(k)}$
4: $\beta^{(k)} = \mathbf{r}_{k+1}^{\mathrm{T}}\mathbf{M}^{-1}\mathbf{t}^{(k+1)}/\mathbf{r}_k^{\mathrm{T}}\mathbf{M}^{-1}\mathbf{r}^{(k)}$
5: $\mathbf{d}^{(k+1)} = \mathbf{M}^{-1}\mathbf{r}^{(k+1)} + \beta^{(k)}\mathbf{d}^{(k)}$
6: $k = k + 1$
while $\mathbf{d}^{(k)2} > \varepsilon$
Return $\mathbf{t}^{(k+1)}$

If the value of $\mathbf{d}^{(k)2}$ is within a predetermined threshold, the iterative procedure is stopped; otherwise, go to step 1.

The Combined PCG and GPU Computing Method for BA Estimation

The problem of BA estimation mainly includes the calculation of reprojection error, Jacobian matrix, preconditioner matrix, and multiplication between matrix and vector.

GPU Accelerated BA Parallel Computing Optimization Method

(1) *Parallel computation optimization of the reprojection errors* **L**

The constant vector represents the reprojection errors of the tie points corresponding to the ground point on its corresponding image, which is only related to the coordinates of the ground points corresponding to the image points and the corresponding image parameters. The reprojection errors of different image points are independent of each other (Figure 3).

To realize the parallel calculation of reprojection error, each thread is responsible for calculating one reprojection. The number of threads is the same as that of reprojections, and each thread completes one reprojection error calculation independently. Then the parallel calculation of reprojection errors is converted into

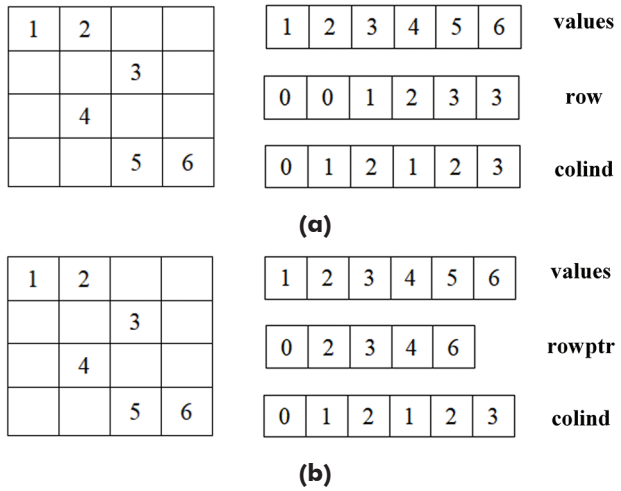

Figure 2. The storage formats for the sparse design matrix (adapted from (Cheng, Tian, and Ma 2018)). (a) Coordinate (COO) format; (b) Compressed Sparse Row (CSR) format.

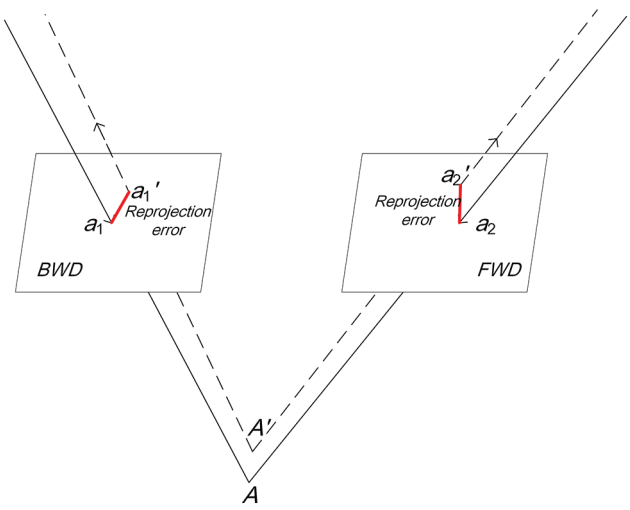

Figure 3. Reprojection errors. BWD represents the backward image, FWD represents the forward image. A represents the ground point coordinate, a1 and a2 represent the image point coordinates on the BWD and FWD images respectively, a_1' and a_2' represent the reprojection coordinates of the image points on the BWD and FWD images, respectively. Reprojection errors are only related to the ground points corresponding to the image points and each image parameters, and image points are independent of each other.

multi-threads to obtain the corresponding reprojection at the same time. The RPC parameters are obtained by the image index, the object coordinates of tie points are located by the image point index, and the image coordinates of tie points are located by the thread index in the projection procedure. Each thread obtains the corresponding parameters from the texture memory, and then according to the reprojection formula, the reprojection errors can be calculated in parallel.

(2) *Parallel computing optimization of the Jacobian matrix* **J** *and preconditioner matrix* **M**

The calculation of the Jacobian matrix **J** can be divided into the solution of image parameters and three-dimensional (3D) point coordinate parameters, i.e., $\mathbf{J} = [\mathbf{J}_c, \mathbf{J}_p]$, to solve the partial derivative $\mathbf{J}_c$ of image parameters and the partial derivative $\mathbf{J}_p$ of 3D point coordinates.

For each image point, the partial derivative matrix $\mathbf{J}_c$ of its corresponding image parameters can be represented by 12 values, and the partial derivative matrix $\mathbf{J}_p$ of corresponding 3D points can be represented by six values. Taking nine scenes of ZY-3 01 satellite images for an example, the number of corresponding ground points is 90 and the number of the image points is 351. The structure of the Jacobian matrix **J** is shown in Figure 4.

Similar to solving the reprojection errors, the parallel solution of the Jacobian matrix J is to establish the relationship between each thread and image parameter and 3D point coordinate. Firstly, the projection values are obtained in the global memory, and then the image parameters are located by the image index in the projection. Then, the 3D point coordinates are obtained from the global memory by the 3D point index in the projection. Finally, the Jacobian matrix J is obtained through the partial derivative formula.

The solution of the preconditioner matrix **M** can be transformed into solving the $\mathbf{J}_c^{\mathrm{T}}\mathbf{J}_c$ and $\mathbf{J}_p^{\mathrm{T}}\mathbf{J}_p$ matrix. The multiplication of the $\mathbf{J}_c^{\mathrm{T}}$ and $\mathbf{J}_c$ matrix is the dot product of the Jc column vector. For example, the value of the first row and second column of the $\mathbf{J}_c^{\mathrm{T}}\mathbf{J}_c$ matrix is the dot product of the first and second columns of the $\mathbf{J}_c$ matrix. Therefore, the product of matrix and matrix is decomposed into the dot product of vector and vector. The dot product between different column vectors is independent and is especially suitable for parallel calculations. The product of each dimension has no effect on the product of other dimensions, which can be calculated by compute unified device architecture's (CUDA's) parallel reduction function. The structure of the $\mathbf{J}_c^{\mathrm{T}}\mathbf{J}_c$ and $\mathbf{J}_p^{\mathrm{T}}\mathbf{J}_p$ matrix is shown in Figure 5.

Besides, the parallel calculation of the $\mathbf{J}_c^{\mathrm{T}}\mathbf{J}_c$ matrix can be carried out directly without storing the $\mathbf{J}_c^{\mathrm{T}}$ matrix. Considering that there are 36 groups of column vector multiplication, every six threads are used to calculate one dimension of the column vector product; that is, every six threads are used to process a row of the $\mathbf{J}_c^{\mathrm{T}}$ matrix and obtain 36 values. Because the 36 values obtained by every six threads, which are one-dimensional of a column vector, thus the CUDA parallel reduction function is used to add up the 36 values obtained by all the six threads in a group to get the result of the whole column vector dot product, that is, the result of the $\mathbf{J}_c^{\mathrm{T}}\mathbf{J}_c$ matrix. Besides, making full use of the symmetry of the $\mathbf{J}_c^{\mathrm{T}}\mathbf{J}_c$ matrix can further reduce about half of the computation and reduce the access to shared memory on the GPU device. Similarly, the parallel calculation of the $\mathbf{J}_c^{\mathrm{T}}\mathbf{J}_c$ matrix can also be calculated according to this method, except that the thread block size is different, that is, nine values obtained by every three threads.

(3) *Parallel computing optimization of the product of the Jacobian matrix* **J** *and constant vector* **L**

The multiplication of the $\mathbf{J}_c^{\mathrm{T}}\mathbf{L}$ matrix can be decomposed into the dot product of column vector and reprojection error vector. The dot product between different column vector and reprojection error vector is independent and can be computed in parallel, and the process of vector dot product can be operated by the CUDA parallel reduction function.

The parallel computation of the $\mathbf{J}_c^{\mathrm{T}}\mathbf{L}$ matrix is carried out directly without storing the $\mathbf{J}_c^{\mathrm{T}}$ matrix. Taking the parallel solution of the $\mathbf{J}_c^{\mathrm{T}}\mathbf{L}$ matrix for an example, a two-dimensional thread block *dimBlock*(n + 1, 2) is defined. Define the thread grid as *dimGrid*(cam_num). Each thread block is responsible for one image, and each thread is used to calculate the product of three values in the $\mathbf{J}_c^{\mathrm{T}}$ matrix and the corresponding reprojection error.

Each thread block contains 2 * (n + 1) threads. Each thread calculates the product of three values in the JcT matrix and the corresponding reprojection error L. The 2 * (n + 1) threads are called

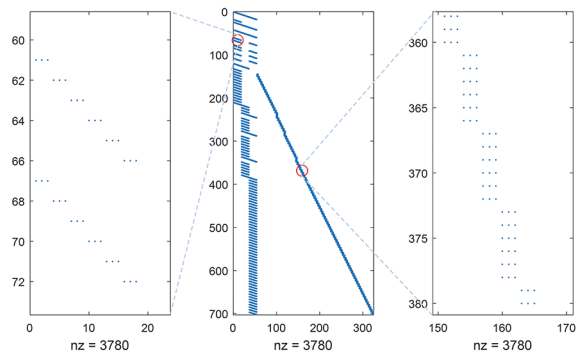

Figure 4. The structure of the Jacobian matrix J. The blue points represent the values of non-zero elements. nz represents the number of non-zero elements.

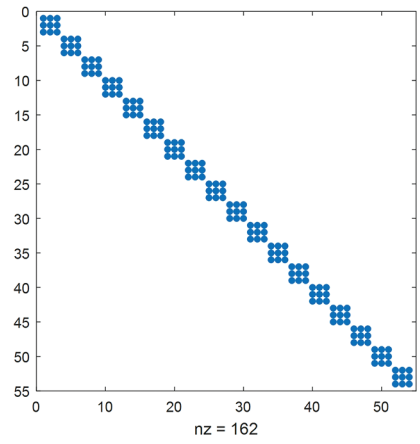

(a)

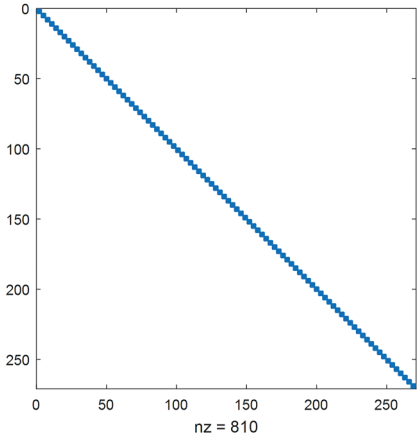

(b)

Figure 5. The structure of the $\mathbf{J}_c^{\mathrm{T}}\mathbf{J}_c$ and $\mathbf{J}_p^{\mathrm{T}}\mathbf{J}_p$ matrix. The blue points represent the values of non-zero elements. (a) The structure of the $\mathbf{J}_c^{\mathrm{T}}\mathbf{J}_c$ matrix; (b) The structure of the $\mathbf{J}_p^{\mathrm{T}}\mathbf{J}_p$ matrix. nz represents the number of non-zero elements.

repeatedly until the JcTL matrix is calculated, and each thread is responsible for calculating three results. Then, 6 * (n + 1) results of 2 * (n + 1) threads are stored into shared memory. Finally, the parallel reduction calculation is completed in shared memory to obtain the $\mathbf{J}_c^{\mathrm{T}}\mathbf{L}$ matrix of each image. The calculation results of the whole $\mathbf{J}_c^{\mathrm{T}}\mathbf{L}$ matrix can be obtained by solving several thread blocks at the same time. Besides, thread synchronization statements should be used. The *_syncthreads* function is used to synchronize threads to ensure that all threads have been stored into the shared memory before performing parallel reduction operations.

GPU Accelerated PCG Parallel Computing Optimization Method

Each step in the PCG method is serial, which involves two times of sparse matrix and vector multiplication, one time of preconditioner matrix and vector multiplication, two times of dot product of two vectors, three times of vector updating, and two times of scalar division. The data-level parallel operation can be used to matrix-vector multiplication, vector-vector multiplication, and vector updating. As a result, the GPU-accelerated PCG method can be used for large-scale BA estimation. The GPU device is used for parallel computation between matrix and vector, and vector and vector, before and during each iteration. The CPU is used to control the iteration cycle, the convergence condition judgment, and the scalar division. NVIDIA's CUDA Sparse Matrix Library cuSPARSE (NVIDIA 2019a) provides operations for sparse matrices, which can be multiplied between vectors by using the *CusparseDcsrmv* function in the cuSPARSE library. The *CublasDdot* function in the cuBLAS (NVIDIA 2019b) library can be used to implement the operation of the dot product of two vectors. The *CublasDaxpy* function in the cuBLAS library is used to update the vector. In this way, the complete PCG method can be realized by using the correlation functions of the cuSPARSE library and the cuBLAS library.

The workflow of the combined PCG and GPU parallel computing method for large-scale BA estimation is shown in Figure 6.

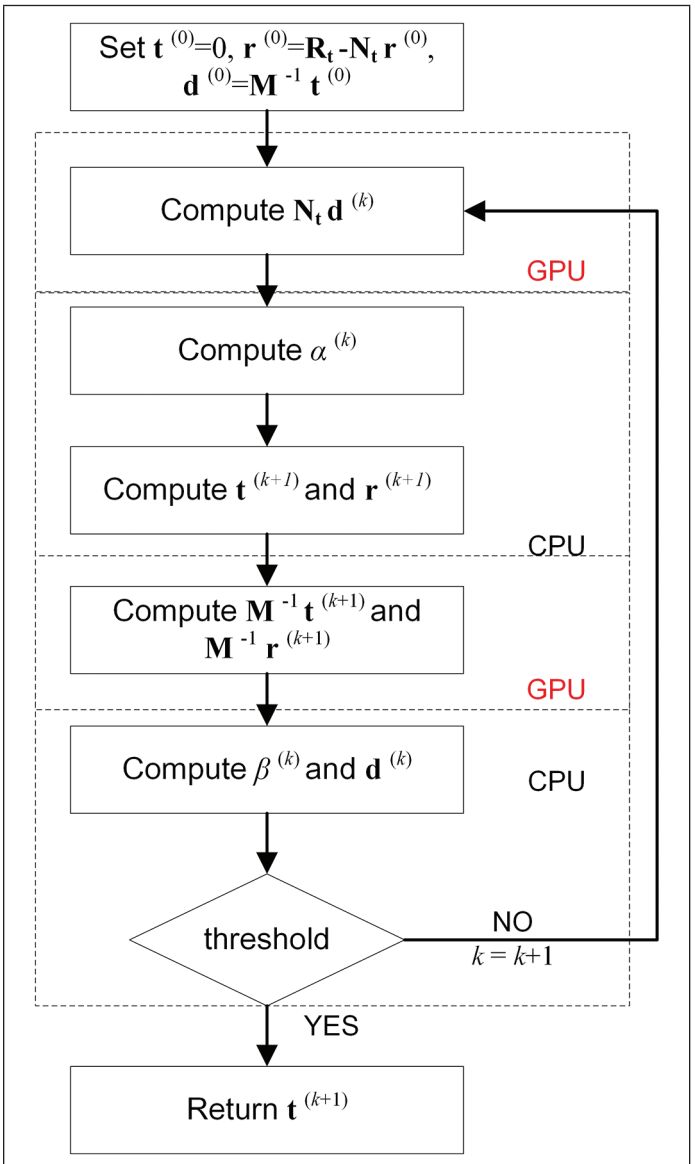

Figure 6. The Preconditioned Conjugate Gradient (PCG) and Graphic Processing Unit (GPU) combined parallel computing method. (The GPU operation is marked in red).

Experiments and Discussion

Study Area and Data Sets

In this study, the BA experiment was carried out using two data sets, namely 132 scenes of Ziyuan-3 (ZY-3) 01 images of Taihu Basin and 829 scenes of ZY-3 01 images of almost the whole Jiangxi Province in China (as shown in Figure 7), which cover areas of about 240 × 310 km and 520 × 650 km, respectively. The software environment used in the experiment was the Windows 10 64-bit operating system, Microsoft Visual Studio 2017 (VC++), and CUDA 10.2. The hardware was a Dell high-performance graphics workstation (the graphics workstation was equipped with a 6-core i7-8700 CPU @ 3.2GHz, 32 GB memory, and an NVIDIA Quadro P2000 professional graphics card with 5 GB global memory).

Two sets of data were used to test the proposed method and the other methods. Details of the data used in this study are provided in

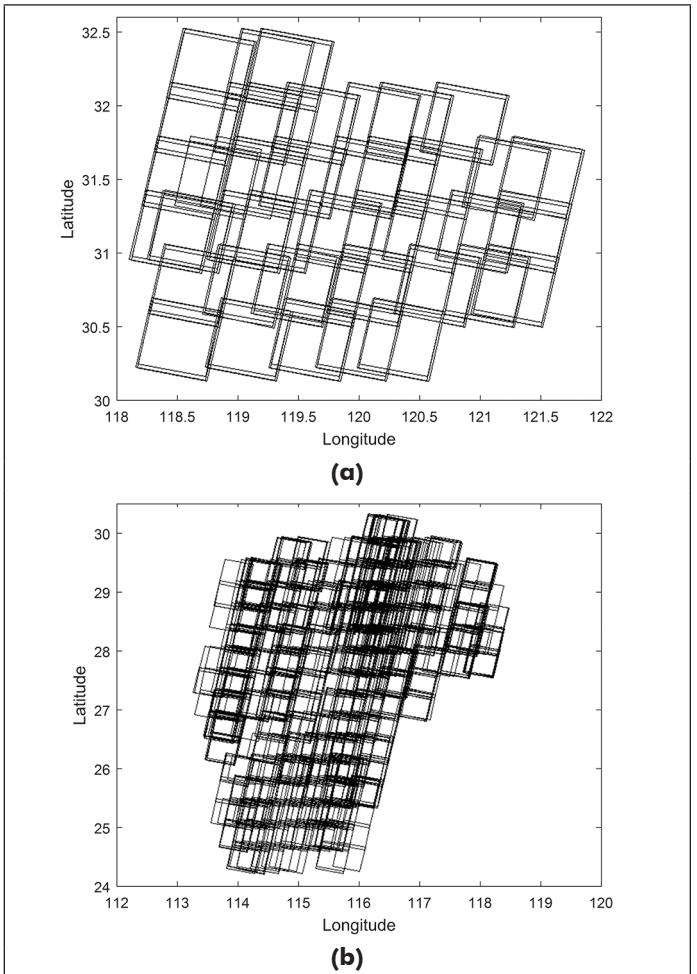

Figure 7. ZY-3 01 satellite image coverage of the two data sets. (a) ZY-3 01 image coverage in the data set A; (b) ZY-3 01 image coverage in the data set B.

Table 1. Data set A contained 132 scenes of ZY-3 01 satellite images, in which the terrain was plain and hilly. Data set B included 829 scenes of ZY-3 01 images, in which the terrain was hilly and mountainous. The ZY-3 01 satellite images of the two areas were captured between 2015 and 2020. Each image was attached with the RPC vendor file. A certain overlap also existed between adjacent images. The survey areas included mountainous, hilly, plain, and other topographic areas, with a maximum and minimum elevation difference of 2500 m.

According to the automatic image-matching methods, such as the scale-invariant feature transform algorithm and k-nearest neighbor matching strategy (the nearest distance threshold is set to 0.8), tie points are acquired from adjacent images, and then the OpenMP parallel matching strategy is adopted to improve the matching efficiency. The number of tie points obtained from the image matching algorithm is very high without a tie point selection strategy and exits some obvious gross errors. In order to solve this issue, we adopted the random sample consensus gross error detection and elimination method, which is effective at reducing the influence of gross errors in the BA results. 63 528 uniform tie points were matched after the use of the above method in the data set A, which cost about one hour, and 158 961 uniform tie points were matched in the data set B, which cost nearly eight hours. The distribution of the tie points of the two data sets is shown in Figure 8.

In order to verify the performance of the proposed method in memory consumption, computational efficiency, and BA accuracy, we compared it with the Single-core CPU and multi-core CPU computing methods. Besides, in order to reduce the statistical error, 10 repeated experiments were carried out and the average value was calculated.

Experimental Results and Discussion

Results of the Memory Consumption Comparison Between the Proposed Method and the Existing Ones

The conventional dense matrix storage format, the CSR sparse matrix storage format, including the single-core CPU, multi-core CPU computing, Ceres-solver, parallel bundle adjustment (PBA) (Wu *et al.* 2011), and the proposed method were used to process the two groups of experimental data. The memory consumption of the five methods was recorded, respectively. The results of the memory consumption during the BA procedure are listed in Table 2.

From Table 2, it can be seen that the memory consumption of the CSR sparse format is clearly lower than that of the conventional full matrix. When the number of images is 132 (data set A), the full matrix storage format needs at least 80 GB of memory in theory, which will eventually lead to the failure of the BA, because of the inability of a standard computer to allocate such a large amount of memory. After using the CSR format of matrix for the normal equation, only about maximum 345 MB memory space is needed to store all the data needed in the BA.

If the number of images continues to increase, the memory required by the full matrix format will continue to increase. When the number of images increases to 829 (data set B), the full matrix storage format needs at least 1000 GB of memory, in theory. After using the CSR format of matrix for the normal equation, only about maximum 562 MB memory space is needed. However, the memory consumption of the PBA and the proposed methods are higher than that of the single-core CPU, multi-core CPU computing, and Ceres-solver methods, because of the introduction of the GPU device. In addition, the memory consumption of the proposed method is lower than that of PBA method, because of Jacobian transpose matrix $\mathbf{J}_c^{\mathrm{T}}$ is not stored, and the matrix $\mathbf{J}_c^{\mathrm{T}}\mathbf{J}_c$ is a symmetric matrix and only needs to calculate the upper triangular. Meanwhile, a temporary vector stored in the shared memory is calculated in each thread for the multiplication of the matrix $\mathbf{J}_c^{\mathrm{T}}$ and matrix $\mathbf{J}_c$, which not only saves global memory consumption, but also improves matrix multiplication computing efficiency.

Comparison of the Computational Time Costs Between the Proposed Method and the Existing Ones

The time costs and computational speedup by the five methods for the two data sets are listed in Table 3. As can be seen from Table 3, when

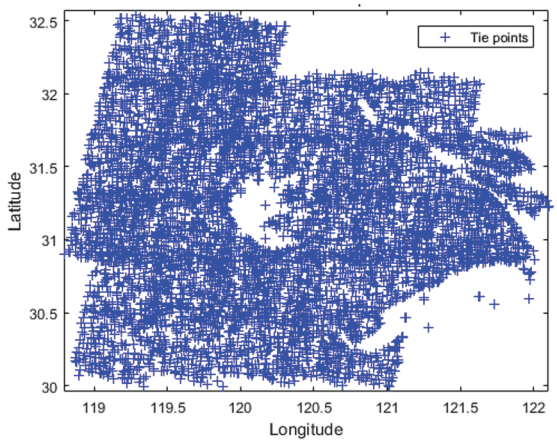

(a)

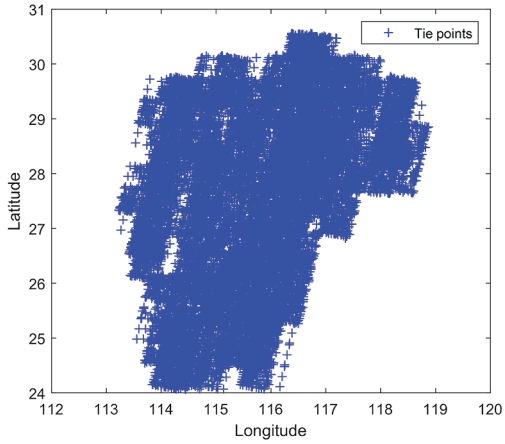

(b)

Figure 8. Distribution of the tie points in the two data sets. (a) Distribution of the tie points in the data set A; (b) Distribution of the tie points in the data set B.

Table 1. Details of the test data sets.

Data Set	Source	Topography	Capture Time	Number of Images	Number of Tie Points
A	ZY-3 01	plain and hilly	2015–2016	132	63 528
B	ZY-3 01	hilly and mountainous	2017–2020	829	158 961

Table 2. Memory consumption of the different methods.

	CSR Sparse Matrix (Units: MB)				
Data Set	Single-core CPU	Multi-core CPU	Ceres-solver	PBA	The Proposed Method
A	184	195	189	356	345
B	340	352	346	583	562

CSR = Compressed Sparse Row; MB = megabytes; CPU = central processing unit; PBA = parallel bundle adjustment.

Table 3. Computational time costs of the different methods (units: seconds).

Data Set	Single-Core CPU	Multi-Core CPU	Ceres-Solver	PBA	The Proposed Method
A	3.21	1.78	2.06	0.56	0.63
B	41.90	13.47	30.15	4.01	4.42

CPU = central processing unit; PBA = parallel bundle adjustment.

the number of images is 132, the conventional full matrix storage method fails in BA because of the limitation of the memory consumption. And the efficiency of the multi-core CPU computing and Ceres-solver methods are higher than that of the single-core CPU computing method, whereas the calculation efficiency of the PBA method is the highest and the proposed method is comparable with PBA method. The computational time costs of the mentioned above five methods are 3.31 s, 1.78 s, 2.06 s, 0.56 s, and 0.63 s in the data set A, and in the data set B, the computational time costs of the five methods are 41.90 s, 13.47 s, 30.15 s, 4.01 s, and 4.41 s, respectively.

As can be seen from Table 4, when the number of images is small (data set A), the computational speedup of the multi-core CPU computing method is a little faster than that of the single-core CPU computing method, namely 1.86 times, while when the number of images is large (data set B), the computational speedup of the multi-core CPU computing method is 3.11 times faster than that of the single-core CPU computing method. But the computational speedup of the proposed method is obviously faster than that of the single-core CPU computing method, namely 5.25 and 9.48 times faster in the two data sets, respectively. In addition, the computational speedup of the PBA method is obvious faster than that of the single-core CPU computing method, namely 5.73 and 10.45 times faster in the two data sets, respectively.

Table 4. Computational speedup of the different methods.

Data Set	Single-Core CPU	Multi-Core CPU	Ceres-Solver	PBA	The Proposed Method
A	1	1.80	1.56	5.73	5.10
B	1	3.11	1.39	10.45	9.48

CPU = central processing unit; PBA = parallel bundle adjustment.

Comparison of BA Accuracies Between the Proposed Method and the Existing Ones

The PBA method and proposed method were found to be superior to the single-core CPU, multi-core CPU computing, and Ceres-solver methods in the computational efficiency. In order to further verify the performance of the proposed method in BA accuracy, we compared the BA accuracy of the above methods. The two groups of data were processed by the methods mentioned above, and the BA accuracy was compared and analyzed.

The BA accuracy was measured by the relative accuracy, i.e., the reprojection residuals of the tie points. Analysis of the reprojection residuals of the tie points can evaluate the accuracy and stability of the BA, which can also reflect the relative geo-positioning accuracy of the images to a certain extent. The BA accuracies of the data set A are shown in Table 5, and the residual errors in the x- and y-directions after the BA by the methods are shown in Figure 9.

The relative geo-positioning accuracy in the data set A is shown in Figure 9, before and after the application of the proposed BA method. The residual errors of the tie points are shown in Table 5, before and after the BA. As can be seen from Table 5, the BA accuracy of the proposed method is comparable to that of the single-core CPU, multi-core CPU computing, and Ceres-solver methods. The maximum reprojection image point residual of the forward intersection used RPC vendor file is 7.973 pixels, the root-mean-square error (RMSE) is 1.725 pixels in the x- (flight) direction, the maximum residual is 10.204 pixels, and the RMSE is 2.466 pixels in the y- (scan) direction. After BA with the proposed method, the maximum residual is 3.787 pixels, the RMSE is 0.561 pixels in the x- (flight) direction, the maximum residual is 7.167 pixels, and the RMSE is 0.752 pixels in the y- (scan) direction. Meanwhile, the BA accuracy of the proposed method is superior to that of the PBA method. The reason is that the threshold value is larger and fewer iterations in the PBA method, which causes the PBA method more efficient than the proposed method.

Conclusions

In this paper, in view of the challenges encountered in the large-scale BA of HRSI without GCPs, we have presented a combined PCG and GPU parallel computing method to estimate the BA results, which can reduce the memory consumption and computational time cost while ensuring the BA accuracy. The PCG method is used to estimate the normal equation, the CSR sparse matrix storage format is adopted to reduce the memory consumption, and a GPU parallel computing method is used to improve the computational efficiency of the proposed approach. Two sets of real data, made up of 132 scenes of ZY-3 01 satellite remote sensing images in Taihu Basin and 829 scenes of ZY-3 01 images almost in the whole of Jiangxi Province of China, were used for the

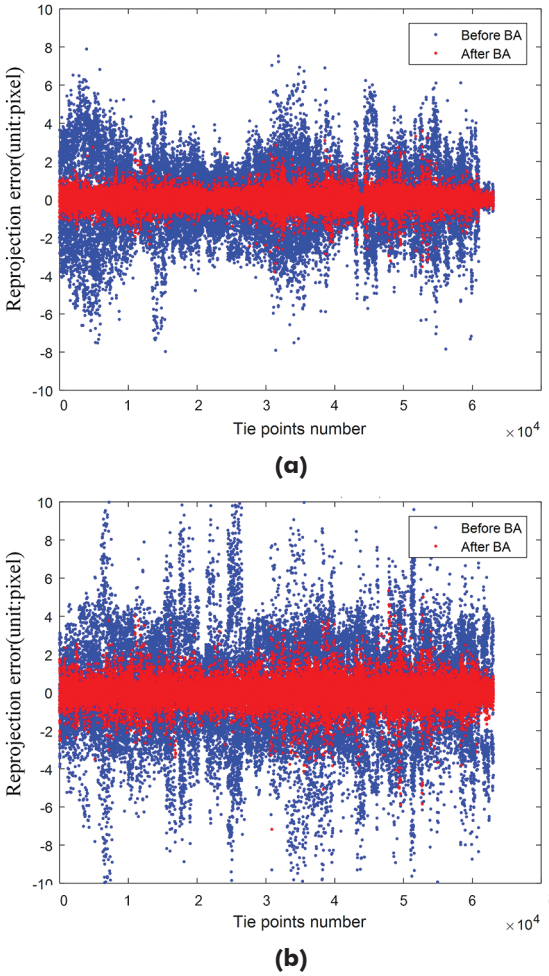

Figure 9. Reprojection error of the tie points in the data set A. (a) Reprojection error in the *x*-direction; (b) Reprojection error in the *y*-direction. BA = bundle adjustment.

Table 5. The root-mean-square error (RMSE) of the different methods (units: pixels)

Data Set	Single-Core CPU			Multi-Core CPU			Ceres-Solver			PBA			The Proposed Method		
	x	*y*	*xy*	*x*	*y*	*xy*	*x*	*y*	*xy*	*x*	*y*	*xy*	*x*	*y*	*xy*
A	0.375	0.630	0.733	0.375	0.630	0.733	0.375	0.630	0.733	0.381	0.674	0.774	0.376	0.631	0.734
B	0.561	0.750	0.936	0.561	0.750	0.936	0.561	0.750	0.936	0.659	0.791	1.03	0.561	0.752	0.938

comparative experiments. Through the comparative analysis of the experimental results, the following conclusions could be drawn:

(1) Compared with the conventional full matrix storage format, the CSR format was found to be able to reduce the memory consumption, and when the number of satellite images reached 829 (data set B), the tie point number reached 158 961, and the memory consumption of the proposed method was 562 MB, while the full matrix storage method failed in the memory application.
(2) The computational speed of the proposed method was found to be much faster than that of the single-core CPU computing method. When the number of images was increased to 132 (data set A), the computational speed of the proposed method was 6.21 times faster than that of the single-core CPU computing method. When the number of images was increased to 829 (data set B), the time costs of the proposed method, the single-core CPU and multi-core CPU computing methods being 4.42 s, 13.47 s, and 41.90 s, and the computational speedup of the proposed method and multi-core CPU computing methods was 9.48 and 3.11 times faster than that of the single-core CPU computing method, respectively, while the full matrix storage method failed in the BA estimation because of the high memory consumption. While the computational efficiency of the proposed method is comparable with that of the PBA method.
(3) The proposed method was able to obtain almost the same BA accuracy as the other methods. When the number of images was 829 in the data set B, the reprojection residuals of the tie points of the proposed method, the single-core CPU, multi-core CPU computing, Ceres-solver, and PBA methods were 0.938, 0.936, 0.936, 0.936, and 1.03 pixels, respectively. Moreover, the BA accuracy of the proposed method is superior to that of the PBA method.

Acknowledgments

The authors would like to thank the editor and anonymous reviewers for their valuable comments, which improved greatly this paper. The work described in this paper was jointly supported by the National Natural Science Foundation of China (project nos. 42171432, 42061055, and 41771483), Shanghai Science and Technology Project (21511103800), Shanghai Municipal Science and Technology Major Project (2021SHZDZX0100) and the Fundamental Research Funds for the Central Universities. The authors would like to thank Jiangxi Natural Resources Surveying, Mapping and Monitoring Institute for providing ZY3-01 satellite imagery of Jiangxi Province.

References

Agarwal, S., N. Snavely, S. Seitz and R. Szeliski. 2010. Bundle adjustment in the large. Pages 29–42 in *Proceedings European Conference on Computer Vision*, held in Heraklion, Crete, 5–11 September 2010.

Agullo, E., C. Augonnet, J. Dongarra, M. Faverge, H. Ltaief, S. Thibault and S. Tomov. 2011. QR factorization on a multicore node enhanced with multiple GPU accelerators. Pages 932–943 in *Proceedings IEEE International Symposium on Parallel and Distributed Processing*, held in Anchorage, Ala., 16–20 May 2011.

Bru, R. and M. Tůma. 2008. Balanced incomplete factorization. *Siam Journal on Scientific Computing* 30:2302–2318. https://doi.org/10.1137/070696088.

Byröd, M. and K. Åström. 2009. Bundle adjustment using conjugate gradients with multiscale preconditioning. Pages 1–10 in *Proceedings British Machine Vision Conference*, held in London, UK, 7–10 September 2009.

Byröd, M. and K. Åström. 2010. Conjugate gradient bundle adjustment. Pages 114–127 in *European Conference on Computer Vision*, held in Heraklion, Crete, 5–11 September 2010.

Cao, N., P. Zhou, X. Wang and G. Li. 2019. Laser altimetry data-aided satellite geometry model refined processing. *Journal of Remote Sensing* 23:291–302. https://doi.org/10.11834/jrs.20197252.

Chen, X., B. Zhang, T. Zhang, H. Guo and M. Cen. 2016. Public DEM-assisted positioning method for Chinese satellite imagery without ground control points. *Acta Geodaetica et Cartographica Sinica* 45:1361–1370.

Cheng, K., J. Tian and R. Ma. 2018. Study on efficient storage format of sparse matrix based on GPU. *Computer Engineering* 44:54–60.

Choudhary, S., S. Gupta and P. Narayanan. 2010. Practical time bundle adjustment for 3d reconstruction on the GPU. Pages 423–435 in *Proceedings European Conference on Computer Vision*, held in Heraklion, Crete, 5–11 September 2010.

D'Angelo, P. and P. Reinartz. 2012. DSM based orientation of large stereo satellite image blocks. Pages 209–214 in *Proceedings XXII ISPRS Congress 2012, ISPRS—International Archives of the Photogrammetry, Remote Sensing and Spatial Information Sciences*, held in Melbourne, Australia, 25 August–1 September 2012.

Fraser, C. S. and H. B. Hanley. 2005. Bias-compensated RPCs for sensor orientation of high-resolution satellite imagery. *Photogrammetric Engineering and Remote Sensing* 71(8):909–915.

Fraser, C. S. and M. Ravanbakhsh. 2009. Geo-reference performance of GEOEYE-1: Early indications of metric performance. Pages 1–6 in *Proceedings ISPRS High-Resolution Earth Imaging for Geospatial Information Workshop*, held in Hannover, Germany, 2–5 June 2009.

Gong, J., M. Wang and B. Yang. 2017. High-precision geometric processing theory and method of high-resolution optical remote sensing satellite imagery without GCP. *Acta Geodaetica et Cartographica Sinica* 46:1255–1261.

Grodecki, J. and G. Dial. 2003. Block adjustment of high-resolution satellite images described by rational polynomials. *Photogrammetric Engineering and Remote Sensing* 69(1):59–68.

Hänsch, R., I. Drude and O. Hellwich. 2016. Modern methods of bundle adjustment on the GPU. Pages 43–50 in *Proceedings ISPRS Annals of Photogrammetry, Remote Sensing and Spatial Information Sciences*, held in Prague, Czech Republic, 12–19 July 2016.

Jiang, Y., G. Zhang, X. Tang, D. Li, T. Wang, W. Huang and L. Li. 2015. Improvement and assessment of the geometric accuracy of Chinese high-resolution optical satellites. *IEEE Journal of Selected Topics in Applied Earth Observations and Remote Sensing* 8(10):4841–4852.

Jiao, N., F. Wang, H. You, M. Yang and X. Yao. 2018. Geometric positioning accuracy improvement of ZY-3 satellite imagery based on statistical learning theory. *Sensors* 18(6):1701.

Liu, S., X. Tong, F. Wang, W. Sun, C. Guo, Z. Ye, Y. Jin, H. Xie and P. Chen. 2016. Attitude jitter detection based on remotely sensed images and dense ground controls: A case study for Chinese ZY-3 satellite. *IEEE Journal of Selected Topics in Applied Earth Observations and Remote Sensing* 9(12):5760–5766.

Liu, X., W. Gao and Z. Hu. 2012. Hybrid parallel bundle adjustment for 3D scene reconstruction with massive points. *Journal of Computer Science and Technology* 27(6):1269–1280.

Ma, Z., X. Wu, L. Yan and Z. Xu. 2017. Geometric positioning for satellite imagery without ground control points by exploiting repeated observation. *Sensors* 17(2):240.

Nathan, B. and M. Garland. 2009. Implementing sparse matrix-vector multiplication on throughput-oriented processors. Pages 1–11 in *Proceedings of the Conference on High Performance Computing Networking*, held in Portland, Ore., 14–20 November 2009.

Noguchi, M., C. Fraser, T. Nakamura, T. Shimono and S. Oki. 2004. Accuracy assessment of QuickBird stereo imagery. *Photogrammetric Record* 19(106):128–137.

NVIDIA. CUDA CUBLAS Library. 2019a. <https://developer.download.nvidia.cn/compute/DevZone/docs/html/CUDALibraries/doc/CUBLAS_Library.pdf, 10 December 2019>.

NVIDIA. CUDA CUSPARSE Library. 2019b. <https://developer.download.nvidia.cn/compute/DevZone/docs/html/CUDALibraries/doc/CUSPARSE_Library.pdf, 10 December 2019>.

Pan, X., T. Jiang, A. Yu, X. Wang and Y. Zhang. 2017. Geo-positioning of remote sensing images with reference image. *Journal of Remote Sensing* 23:673–684.

Peng, J., J. Liu and H. Wei. 2021. A scalable parallel preconditioned conjugate gradient method for bundle adjustment. *Applied Intelligence* 1–13.

Poli, D., L., Zhang and A. Gruen. 2004. SPOT-5/HRS stereo images orientation and automated DSM generation. Pages 421–432 in *Proceedings ISPRS Annals of Photogrammetry, Remote Sensing and Spatial Information Sciences*, held in Istanbul, Turkey Republic, 12–23 July 2004.

Song, W., S. Liu, X. Tong, C. Niu, Z. Ye and Y. Jin. 2021. Combined geometric positioning and performance analysis of multi-resolution optical imageries from satellite and aerial platforms based on weighted RFM bundle adjustment. *Remote Sensing* 13:620.

Sun, Y., L. Zhang, B. Xu and Y. Zhang. 2019. Method and GCP-independent block adjustment for ZY-3 satellite images. *Journal of Remote Sensing* 23:205–214.

Tang, X., G. Zhang, X. Zhu, H. Pan, Y. Jiang, P. Zhou and X. Wang. 2013. Triple linear-array image geometry model of ZiYuan-3 surveying satellite and its validation. *International Journal of Image and Data Fusion* 4:33–51.

Tao, C. V. and Y. Hu. 2001. A comprehensive study of the rational function model for photogrammetric processing. *Photogrammetric Engineering and Remote Sensing* 67(12):1347–1357.

Tong, X., Q. Fu, S. Liu, H. Wang, Z. Ye, Y. Jin, P. Chen, X. Xu, C. Wang, S. Liu, Z. Hong and K. Luan. 2020. Optimal selection of virtual control points with planar constraints for large-scale block adjustment of satellite imagery. *Photogrammetric Record* 35(10):487–508.

Tong, X., L. Li, S. Liu, Y. Xu, Z. Ye, Y. Jin, F. Wang and H. Xie. 2015a. Detection and estimation of ZY-3 three-line array image distortions caused by attitude oscillation. *ISPRS Journal of Photogrammetry and Remote Sensing* 101(3):291–309.

Tong, X., S. Liu and Q. Weng. 2010. Bias-corrected rational polynomial coefficients for high accuracy geo-positioning of QuickBird stereo imagery. *ISPRS Journal of Photogrammetry and Remote Sensing* 65(2):218–226.

Tong, X., S. Liu and Q. Weng. 2009. Geometric processing of QuickBird stereo imageries for urban land use mapping: A case study in Shanghai, China. *IEEE Journal of Selected Topics in Applied Earth Observations and Remote Sensing* 2(2):61–66.

Tong, X., Y. Xu, Z. Ye, S. Liu, X. Tang, L. Li, H. Xie and J. Xie. 2015b. Attitude oscillation detection of the ZY-3 satellite by using multispectral parallax images. *IEEE Transactions on Geoscience and Remote Sensing* 53(6):3522–3534.

Toutin, T. and P. Cheng. 2000. Demystification of IKONOS. *Earth Observation Magazine* 9:17–21.

Wang, M., B. Yang, D. Li and Y. Pi. 2017. Technologies and applications of block adjustment without control for ZY-3 images covering China. *Geomatics and Information Science of Wuhan University* 42(4):427–433.

Wathen, A. and D. Silvester. 1993. Fast iterative solution of stabilised Stokes systems. Part I: Using simple diagonal preconditioners. *SIAM Journal on Numerical Analysis* 30(3):630–649.

Wu, C., S. Agarwal, B. Curless and S. Seitz. 2011. Multicore bundle adjustment. Pages 3057–3064 in *Proceedings of the IEEE Conference on Computer Vision and Pattern Recognition*, held in Colorado Springs, Colo., 20–25 June 2011.

Yang, B., M. Wang, W. Xu, D. Li and Y. Pi. 2017. Large-scale block adjustment without use of ground control points based on the compensation of geometric calibration for ZY-3 images. *ISPRS Journal of Photogrammetry and Remote Sensing* 134:1–14.

Yao, X. and H. You. 2018. Multi-observed block adjustment for satellite images without ground control points. *Remote Sensing Technology and Application* 33:555–562.

Zhang, G., B. Jiang, T. Wang, Y. Ye and X. Li. 2021. Combined block adjustment for optical satellite stereo imagery assisted by spaceborne SAR and laser altimetry data. *Remote Sensing* 13:3062.

Zhang, Y., Y. Wan, X. Huang and X. Ling. 2016. DEM-assisted RFM block adjustment of pushbroom nadir viewing HRS imagery. *IEEE Transactions on Geoscience and Remote Sensing* 54(2):1025–1034.

Zhang, Y., M. Zheng, X. Xiong and J. Xiong. 2014. Multistrip bundle block adjustment of ZY-3 satellite imagery by rigorous sensor model without ground control point. *IEEE Geoscience and Remote Sensing Letters* 12(4):865–869.

Zheng, M., Y. Zhang, S. Zhou, J. Zhu and X. Xiong. 2016. Bundle block adjustment of large-scale remote sensing data with block-based sparse matrix compression combined with preconditioned conjugate gradient. *Computers and Geosciences* 92(7):70–78.

Zheng, M., S. Zhou, X. Xiong and J. Zhu. 2017. A new GPU bundle adjustment method for large-scale data. *Photogrammetric Engineering and Remote Sensing* 83:633–641.

Zhou, P., X. Tang, Z. Wang, N. Cao and X. Wang. 2018. SRTM-assisted block adjustment for stereo pushbroom imagery. *Photogrammetric Record* 33(161):49–65.

IN-PRESS ARTICLES

Oussama Mezouar, Fatiha Meskine, Issam Boukerch. Automatic Satellite Images Ortho-rectification using K-means based Cascaded Meta-heuristic Algorithm.

Yuanyang Lin, Jing He, Gang Liu, Biao Mou, Bing Wang, and Rao Fu. UAS-based multi-temporal rice plant height change prediction.

Bo Xu, Daiwei Zhang, Han Hu, Qing Zhu, Qiang Wang, Xuming Ge, Min Chen, Yan Zhou. Spherical Hough Transform for Robust Line Detection toward a 2D-3D Integrated Mobile Mapping System.

Xinyan Pang, Na Ren, Changqing Zhu, Shuitao Guo, Ying Xiong. Blind and Robust Watermarking Algorithm for Remote Sensing Images Resistant to Geometric Attacks.

Zhikang Lin, Wei Liu, Yulong Wang, Yan Xu, Chaoyang Niu. Change Detection in SAR Images through Clustering Fusion Algorithm and Deep Neural Networks.

Hongbin Luo, Wanqiu Zhang, Cairong Yue, and Si Chen. Strategies for Forest Height Estimation by High-Precision DEM Combined with Short-Wavelength PolInSAR TanDEM-X.

Yunping Chen, Yue Yang, Lei Hou, Kangzhuo Yang, Jiaxiang Yu, and Yuan Sun. High-Resolution Aerosol Optical Depth Retrieval in Urban Areas Based on Sentinel-2.

Xiaoguang Ruan, Fanghao Yang, Meijing Guo, and Chao Zou. 3D Scene Modeling Method and Feasibility Analysis of River Water-Land Integration.

Identification of Drought Events in Major Basins of Africa from GRACE Total Water Storage and Modeled Products

Ayman M. Elameen, Shuanggen Jin, and Daniel Olago

Abstract

Terrestrial water storage (TWS) plays a vital role in climatological and hydrological processes. Most of the developed drought indices from the Gravity Recovery and Climate Experiment (GRACE) over Africa neglected the influencing roles of individual water storage components in calculating the drought index and thus may either underestimate or overestimate drought characteristics. In this paper, we proposed a Weighted Water Storage Deficit Index for drought assessment over the major river basins in Africa (i.e., Nile, Congo, Niger, Zambezi, and Orange) with accounting for the contribution of each TWS component on the drought signal. We coupled the GRACE data and WaterGAP Global Hydrology Model through utilizing the component contribution ratio as the weight. The results showed that water storage components demonstrated distinctly different contributions to TWS variability and thus drought signal response in onset and duration. The most severe droughts over the Nile, Congo, Niger, Zambezi, and Orange occurred in 2006, 2012, 2006, 2006, and 2003, respectively. The most prolonged drought of 84 months was observed over the Niger basin. This study suggests that considering the weight of individual components in the drought index provides more reasonable and realistic drought estimates over large basins in Africa from GRACE.

Introduction

Droughts have increased in frequency and severity due to climate change throughout the world's river basins in recent decades (Forootan *et al.* 2019). According to the sixth assessment report of the International Panel for Climate Change (IPCC), global temperatures have risen by ~1°C since industrialization, which may further amplify by 1.5°C between 2030 and 2050 as a result of human activities (IPCC 2018). As the population grows and water demand increases, droughts are triggered and aggravated by anthropogenic activities such as deforestation and the construction of dams (Schlosser *et al.* 2014; AghaKouchak 2015; Omer *et al.* 2020; Sarfo *et al.* 2022). To prioritize adaptation actions in global hot spots, it is essential to characterize droughts.

Although the continent has abundant water resources with meeting its ecological and agricultural needs, climatic extremes are becoming increasingly perilous, endangering the valuable water supply and millions of lives on the continent (Masih *et al.* 2014; IPCC 2022). Two of the biggest drought tragedies ever documented in history occurred in the Sahel region in 2007 and the Nile basin in 1984. These droughts caused the death of approximately 750 000 people (Vicente-Serrano *et al.* 2012). Future projections indicate that the probability of drought occurrence will increase across the entire African continent, leading to significant regional implications (Ahmadalipour and Moradkhani 2018; IPCC 2022). Additionally, excessive water demand may lead to the overuse of freshwater resources, which might result in disputes among water users during dry spells. This may increase the risk of hydro-political tension in Africa, as the Transboundary Rivers represent 64% of the entire region's landmass (United Nations Environment Program 2010). Monitoring the drought situation in Africa is crucial for prioritizing adaptations to avert water scarcity and disputes.

Long and uninterrupted in situ hydro-climatic observations are required for drought monitoring. Yet Africa's land-based observation network has been deteriorating with time, having only one-eighth of the minimum density required by the World Meteorological Organization and with only 22% of stations fully meeting the Global Climate Observing System requirements (Dobardzic *et al.* 2019). Due to the insufficiency of in situ data records in Africa, monitoring hydrological drought in the continent's basins has been limited (Ferreira *et al.* 2018). Additionally, a substantial financial and political commitment is required to record and share in situ observations, both of which are frequently missing. Remote sensing observations represent an alternative source to counter data deficiencies in many data-poor regions worldwide. Moreover, satellite-borne sensors have featured as an effective tool for tracking droughts, considering their capacity to offer regional-to-global coverage (Jiao *et al.* 2021).

Several remote sensing–based products have been used globally to assess and detect drought situations. Among these are Moderate Resolution Imaging Spectroradiometer (MODIS)–based evapotranspiration, soil moisture from Sentinel-1 and the Soil Moisture Active Passive radiometer, and the Normalized Difference Vegetation Index from Landsat (West *et al.* 2019; Modanesi *et al.* 2020). Although these measurements could deliver valuable information about agricultural and meteorological droughts, the task of assessing hydrological drought remains daunting (Papa *et al.* 2022) since they can capture only surface and shallow subsurface conditions. Also, it is problematic to evaluate droughts based only on surface measurements (e.g., precipitation and soil moisture), as the reduction of water from the deepest aquifers may continue even after the surface storage has dried up (Leblanc *et al.* 2009). After launching the Gravity Recovery and Climate Experiment (GRACE) satellite mission in 2002, the potential time-variable gravity measurement offered an integrated perspective for drought monitoring since it can capture vertically integrated terrestrial water storage (TWS)

Ayman M. Elameen is with the School of Remote Sensing and Geomatics Engineering, Nanjing University of Information Science and Technology, Nanjing 210044, China.

Shuanggen Jin is with the School of Remote Sensing and Geomatics Engineering, Nanjing University of Information Science and Technology, Nanjing 210044, China; the School of Surveying and Land Information Engineering, Henan Polytechnic University, Jiaozuo 454000, China; and Shanghai Astronomical Observatory, Chinese Academy of Science, Shanghai 200030, China (sgjin@nuist.edu.cn; sg.jin@yahoo.com).

Daniel Olago is with the Department of Earth and Climate Sciences, University of Nairobi, Nairobi 00100, Kenya..

Contributed by Dongdong Wang, June 1, 2022 (sent for review September 14, 2022; reviewed by Alper Yilmaz, Vagner Goncalves Ferreira,).

Photogrammetric Engineering & Remote Sensing
Vol. 89, No. 4, April 2023, pp. 221–232.
0099-1112/22/221–232

doi: 10.14358/PERS.22-00092R2

Lightweight Parallel Octave Convolutional Neural Network for Hyperspectral Image Classification

Dan Li, Hanjie Wu, Yujian Wang, Xiaojun Li, Fanqiang Kong, and Qiang Wang

Abstract

*Although most deep learning-based methods have achieved excellent performance for hyperspectral image (HSI) classification, they are often limited by complex networks and require massive training samples in practical applications. Therefore, designing an efficient, lightweight model to obtain better classification results under small samples situations remains a challenging task. To alleviate this problem, a novel, lightweight parallel octave convolutional neural network (*LPOCNN*) for HSI classification is proposed in this paper. First, the HSI data is preprocessed to construct two three-dimensional (3D) patch cubes with different spatial and spectral scales for each central pixel, removing redundancy and focusing on extracting spatial features and spectral features, respectively. Next, two non-deep parallel branches are created for the two inputs, which design octave convolution rather than classical 3D convolution to facilitate light weighting of the model. Then two-dimensional convolutional neural network is used to extract deeper spectral-spatial features when fusing spectral-spatial features from different parallel layers. Moreover, the spectral-spatial attention is designed to promote the classification performance even further by adaptively adjusting the weights of different spectral-spatial features according to their contribution to classification. Experiments show that our suggested LPOCNN acquires a significant advantage on classification performance over other competitive methods under small sample situations.*

Introduction

Hyperspectral image (HSI) is acquired by an imaging spectrometer with high spectral resolution and contains multiple dense and continuous narrow band his. HSI is a three-dimensional cube that records both spatial and rich spectral information of ground objects and accurately reflects the spatial and spectral characteristics of the target (Vantaram *et al.* 2015; Zabalza *et al.* 2015; Zhang *et al.* 2019). Therefore, the advantage of providing rich spectral-spatial information makes HSI play a rather important role in various fields, such as land cover classification (Hosseini *et al.* 2012; Khan *et al.* 2018), mineral exploration (Du *et al.* 2016; Peyghambari and Zhang 2021), military reconnaissance (Bitar *et al.* 2019), and environmental detection (Ghamisi *et al.* 2018; Yu *et al.* 2021a). In these above HSI applications, there is such a fundamental problem as HSI classification (Chen *et al.* 2014; Fauvel *et al.* 2013; He *et al.* 2018; Prabukumar *et al.* 2018), aiming to classify all the pixels in HSI to confirm their true categories.

In the past decades, various traditional HSI classifiers based on manually extracted features have been introduced. However, HSI classification faces a challenge called "curse of dimensionality" because of the high-dimensional nature of HSI. To address the above challenge, researchers propose a series of dimensionality reduction methods for HSI classification, e.g., principal component analysis (PCA) (Kang *et al.* 2017), the maximum noise fraction (He *et al.* 2019), and band selection (Wang *et al.* 2017). These dimensionality reduction algorithms mentioned above map the high-dimensional HSI to the lower-dimensional feature space while retaining distinguishability between different land-cover classes. In general, there are two main classes of traditional HSI classifiers according to whether they use spatial context information: (1) HSI classification methods based on spectral information only, e.g., random forest (Crawford *et al.* 2004; Ham *et al.* 2005; Xia *et al.* 2016b), extreme learning machine (Yu *et al.* 2021b), and support vector machines (SVM) (Heydari and Mountrakis 2019; Tarabalka *et al.* 2010; Xia *et al.* 2016a; Yan *et al.* 2013); (2) HSI classification methods based on spectral-spatial information, e.g., extended morphological profiles (Dalla Mura *et al.* 2011; Wu *et al.* 2017), SVM with composite kernels (SVMCK) (Camps-Valls *et al.* 2006; Marconcini *et al.* 2009; Peng *et al.* 2015), the joint sparse representation classifiers (Cao *et al.* 2019), and 3D-Gabor phase coding classifiers (Chen *et al.* 2021). However, all these classification algorithms mentioned above require hand-designed feature extraction strategies to obtain easily distinguishable features, and the performance of these classification algorithms also depends on the researchers' experience working in the field of HSI classification. Therefore, designing an effective traditional hyperspectral classification algorithm takes a lot of time.

Recently, deep learning-based methods (Audebert *et al.* 2019; Guo and Zhu 2021; Liu *et al.* 2017; Ma *et al.* 2015) have demonstrated excellent practical achievements for HSI classification since they can automatically learn nonlinear deep semantic features of complex data without manually designing feature extraction strategies. The stacked autoencoder (SAE) (Chen *et al.* 2014) pioneers his exploration of deep learning algorithms for HSI classification, followed closely by deep belief networks (DBN) (Chen *et al.* 2015). However, the classification results achieved are limited when applying SAE and DBN to HSI classification, because they require the input data format to be one-dimensional, resulting in a large amount of discarded useful information. To solve this problem, convolutional neural network (CNN) (Chen *et al.* 2017; Hu *et al.* 2015; Liu *et al.* 2018; Yu *et al.* 2018) is applied to HSI classification by researchers. It can automatically extract deep spectral and spatial features with multiple convolutional layers and achieve good classification results when applied to HSI classification. At first, researchers apply two-dimensional CNN (2DCNN) (Bhatti *et al.* 2022; Salman and Yuksel 2016; Song *et al.* 2018) to HSI classification, and then propose three-dimensional CNN (3DCNN) (Feng *et al.* 2019; Kang and Kim 2021; Liu *et al.* 2018) that is more suitable for three-dimensional hyperspectral images. 3DCNN can select a 3D block around the central pixel as the input of this network and can explore 3D spectral-spatial features of HSI concurrently. Nevertheless, there is a problem of gradient disappearance when training deeper 2DCNN or 3DCNN. To alleviate this problem, residual learning is introduced into CNN-based HSI classification networks. The spectral–spatial residual network (SSRN)

Dan Li, Hanjie Wu, Yujian Wang, and Fanqiang Kong are with the College of Astronautics, Nanjing University of Aeronautics and Astronautics, Nanjing 210016, China (wuhanjie@nuaa.edu.cn).

Xiaojun Li is with the National Key Laboratory Science and Technology Space Microwave, China Academic Space Technology, Xian 710018, China.

Qiang Wang is with the Control Science and Engineering, Harbin Institute of Technology, Harbin 150001, China.

Contributed by Hongyan Zhang, August 21, 2022 (sent for review September 14, 2022; reviewed by Alper Yilmaz, Jiaqi Zou).

Photogrammetric Engineering & Remote Sensing
Vol. 89, No. 4, April 2023, pp. 233–243.
0099-1112/22/233–243

doi: 10.14358/PERS.22-00111R2

Call for *PE&RS* Special Issue Submissions

Innovative Methods for Geospatial Data using Remote Sensing and GIS

Internationally comparable data is a global need for managing resources, monitoring current trends and taking actions for sustainable living. Even though there has been a significant progress on geospatial data availability, extensive data gaps are still a major problem for general assessment and supervise the progress through the years. According to United Nations 2022 The Sustainable Development Goals Report, while health and energy sectors have the highest data available, limited data available for climate action.

The COVID-19 crisis has also shown that there are innovative data collection methods utilizing information and computer technologies. However, only 5% of the countries have benefit from remote sensing technologies to measure the impact of COVID-19. Additionally, novel approaches such as artificial intelligence should be used in conjunction with assessments to make sure they are put to use for critical situations.

The recent developments in remote sensing, geographic information systems and ICT have provided a wide accessibility to create geospatial data for various purposes. The proposed special issue focuses on *"Innovative Methods for Geospatial Data using Remote Sensing and GIS" for wide range of applications. This special issue aims to bring researchers to share knowledge and their expertise about innovative methods to contribute to fill data gaps around the world for a better future.*

The proposed special issue aims to contributes ASPRS's key mission on 'Simplify and promote the use of image-based geospatial technologies for the end-user', 'Promote collaboration between end users and geospatial experts to match data and technology to applications and solutions' and 'promote the transfer of geospatial data and information technology to developing nations' by providing innovative methods to create geospatial data using remote sensing and geographic information systems utilizing state-of-the-art developments and solutions.

Deadline for Manuscript Submission—July 1, 2023

Submit your Manuscript to http://asprs-pers.edmgr.com

Guest Editors

Dr. Tolga Bakirman, bakirman@yildiz.edu.tr , *Yildiz Technical University, Department of Geomatic Engineering*, Davutpasa Campus, 34220 Esenler-Istanbul/Turkey

Dr. George Arampatzis, garampatzis@pem.tuc.gr, *Technical University Crete, School of Production Engineering & Management*, 73100 Chania – Crete/Greece

Model-Driven Precise Degradation Analysis Method of Highway Marking Using Mobile Laser Scanning Point Clouds

Ruifeng Ma, Xuming Ge, Qing Zhu, Xin Jia, Huiwei Jiang, Min Chen, and Tao Liu

Abstract

Highway markings (HMs) are representative elements of inventory digitalization in highway scenes. The accurate position, semantics, and maintenance information of HMs provide significant support for the intelligent management of highways. This article presents a robust and efficient approach for extracting, reconstructing, and degrading analyzing HMs in complex highway scenes. Compared with existing road marking extraction methods, not only can extract HMs in presence of wear and occlusion from point clouds, but we also perform a degradation analysis for HMs. First, the HMs candidate area is determined accurately by sophisticated image processing. Second, the prior knowledge of marking design rules and edge-based matching model that leverages the standard geometric template and radiometric appearance of HMs is used for accurately extracting and reconstructing solid lines and nonsolid markings of HMs, respectively. Finally, two degradation indicators are constructed to describe the completeness of the marking contour and consistency within the marking. Comprehensive experiments on two existing highways revealed that the proposed methods achieved an overall performance of 95.4% and 95.4% in the recall and 93.8% and 95.5% in the precision for solid line and nonsolid line markings, respectively, even with imperfect data. Meanwhile, a database can be established to facilitate agencies' efficient maintenance.

Introduction

Three-dimensional (3D) spatial virtual construction technology is of great significance for the development of smart highways. The accurate position and semantics of highway markings (HMs) provide significant support for highway digital operation, maintenance, and intelligent management. Highway marking is a representative element for the digitization of highway inventory and is also necessary to realize highway alignment extraction and modeling (Zhou *et al.* 2021).

In recent years, airborne light detection and ranging (lidar) scanning technologies have been widely used to acquire dense point clouds for various applications, such as 3D city modeling and digital elevation model generation (Guan *et al.* 2014; Yang *et al.* 2017; Zhu *et al.* 2022). However, mobile laser scanning (MLS) efficiently, reliably, and cost-effectively acquires high-density, high-precision, and multi-detail 3D point clouds of corridor scenes (Guan *et al.* 2014; Mi *et al.* 2021; Rastiveis *et al.* 2019; Wang *et al.* 2017; Yan *et al.* 2016; Zai *et al.* 2018), which provides convenience for road surface features (e.g., road marking) extraction and reconstruction for timely road maintenance. An MLS is the integration of several devices, including a laser scanner, a global navigation satellite system (GNSS), an inertial measurement unit (IMU), high-resolution cameras, and a computer control device (Kumar *et al.* 2014). In complex highway scenes, due to severe noise, diverse terrain, and the existence of varying wear, occlusion, robust extraction, and reconstruction of HMs using MLS point clouds still have some unsolved problems in current engineering applications (Jung *et al.* 2019; Mi *et al.* 2021).

A great number of methods discussed in the section "Related Works" have been developed for automatic extraction, classification, and reconstruction based on the geometric features and reflection intensity of the MLS point clouds in corridor scenes, which also improved the automation level of HM extraction to a certain extent. However, most methods including raster-based and point-based both currently use bottom-up strategies, which are sensitive to imperfect raw data and difficult to apply for extracting HMs in complex highway scenes. Moreover, in existing methods, there are few reports on conducting a degradation analysis of the highway markings for further maintenance. This study presents an automatic method for extraction and degradation analysis of HMs by MLS point clouds. The proposed method extracts the candidate area of solid lines and nonsolid markings (including dashed lines and various types of complicated arrow markings) from the intensity feature map generated by pavement point clouds. The prior knowledge of marking design rules and edge-based matching is used for accurately extracting and reconstructing solid lines and nonsolid markings, respectively. Two degradation indicators are constructed to describe the completeness of the marking contour and consistency within the marking, which can be useful for authorities to further assess maintenance. The main contributions of the proposed method are as follows:

(1) A new framework that not only achieves the fine reverse modeling of HMs at the digital dimension but also implemented degradation analysis for actual operation of highway marking is presented.
(2) After projecting the MLS point clouds to feature map, a dynamic threshold segmentation is designed to identify candidates for highway marking. Within the candidate, the model-driven strategy and the road marking design rules are adopted to accurately extract and reconstruct highway marking in terms of good robustness to severe noise, the uneven density of the point clouds, wear, and occlusion of highway markings.
(3) Two degradation indicators from different aspects are constructed to reflect the condition of marking objects for further maintenance.

The remainder of this paper is organized as follows. After introducing the related work in the section "Related Works", we describe the

Ruifeng Ma, Xin Jia, and Tao Liu are with the Faculty of Geomatics, Lanzhou Jiaotong University, Lanzhou, China.

Ruifeng Ma, Xuming Ge, Qing Zhu, Xin Jia, and Min Chen are with the Faculty of Geosciences and Environmental Engineering, Southwest Jiaotong University, Chengdu, China. (xuming.ge@swjtu.edu.cn).

Huiwei Jiang is with the National Geomatics Center of China, Beijing, 100830, China.

Ruifeng Ma is also with the Academician Expert Workstation of Gansu Dayu Jiuzhou Space Information Technology CO., Ltd.

Min Chen is also with the Key Laboratory of Urban Land Resources Monitoring and Simulation, Ministry of Natural Resources, Shenzhen, China.

Contributed by Rongjun Qin, September 19, 2022 (sent for review November 7, 2022; reviewed by Mustafa Zeybek, Shengjun Tang).

Photogrammetric Engineering & Remote Sensing
Vol. 89, No. 4, April 2023, pp. 245–258.
0099-1112/22/245–258

doi: 10.14358/PERS.22-00119R2

WHO'S WHO IN ASPRS

Founded in 1934, the American Society for Photogrammetry and Remote Sensing (ASPRS) is a scientific association serving thousands of professional members around the world. Our mission is to advance knowledge and improve understanding of mapping sciences to promote the responsible applications of photogrammetry, remote sensing, geographic information systems (GIS) and supporting technologies.

BOARD OF DIRECTORS

BOARD OFFICERS

President
Lorraine B. Amenda, PLS, CP
Towill, Inc

President-Elect
Bandana Kar
Oak Ridge National Lab

Vice President
Amr Abd-Elrahman
University of Florida

Past President
Christopher Parrish, Ph.D
Oregon State University

Treasurer
John McCombs
NOAA

Secretary
Harold Rempel
ESP Associates, Inc.

COUNCIL OFFICERS

ASPRS has six councils. To learn more, visit https://www.asprs.org/Councils.html.

Sustaining Members Council
Chair: Ryan Bowe
Deputy Chair: Melissa Martin

Technical Division Directors Council
Chair: Hope Morgan
Deputy Chair:

Standing Committee Chairs Council
Chair:
Deputy Chair:

Early-Career Professionals Council
Chair: Youssef Kaddoura
Deputy Chair:

Region Officers Council
Chair: Demetrio Zourarakis
Deputy Chair: Jason Krueger

Student Advisory Council
Chair: Oscar Duran
Deputy Chair:

TECHNICAL DIVISION OFFICERS

ASPRS has seven professional divisions. To learn more, visit https://www.asprs.org/Divisions.html.

Geographic Information Systems Division
Director: Denise Theunissen
Assistant Director: Jin Lee

Lidar Division
Director: Ajit Sampath
Assistant Director: Mat Bethel

Photogrammetric Applications Division
Director: Ben Wilkinson
Assistant Director: Hank Theiss

Primary Data Acquisition Division
Director: Srini Dharmapuri
Assistant Director: Ravi Soneja

Professional Practice Division
Director: Hope Morgan
Assistant Director: Matt Elious

Remote Sensing Applications Division
Director: Tao Liu
Assistant Director: Indu Jeyachandran

Unmanned Autonomous Systems (UAS)
Director: Jacob Lopez
Assistant Director: Bahram Salehi

REGION PRESIDENTS

ASPRS has 13 regions to serve the United States. To learn more, visit https://www.asprs.org/regions.html.

Alaska Region

Cascadia Region
Jimmy Schulz

Eastern Great Lakes Region
Craig Fry

Florida Region
Matt LaLuzerne

Gulf South
Cody Condron

Heartland Region
Whit Lynn

Mid-South Region
David Hughes

North Atlantic Region
Kurt Lutz

Northeast Region

Pacific Southwest Region
Omar Mora

Potomac Region
Jason Brown

Rocky Mountain Region
Trent Casi

Western Great Lakes Region
Adam Smith

SUSTAININGMEMBERS

ACI USA Inc.
Weston, Florida
https://acicorporation.com/
Member Since: 2/2018

Aerial Services, Inc.
Cedar Falls, Iowa
www.AerialServicesInc.com
Member Since: 5/2001

Airworks Solutions Inc.
Boston, Massachusetts
Member Since: 3/2022

Applanix
Richmond Hill, Ontario, Canada
http://www.applanix.com
Member Since: 7/1997

Ayres Associates
Madison, Wisconsin
www.AyresAssociates.com
Member Since: 1/1953

Cardinal Systems, LLC
Flagler Beach, Florida
www.cardinalsystems.net
Member Since: 1/2001

CT Consultants
Mentor, Ohio
Member Since: 3/2022

Dewberry
Fairfax, Virginia
www.dewberry.com
Member Since: 1/1985

Esri
Redlands, California
www.esri.com
Member Since: 1/1987

GeoCue Group
Madison, Alabama
http://www.geocue.com
Member Since: 10/2003

Geographic Imperatives LLC
Centennial, Colorado
Member Since: 12/2020

GeoWing Mapping, Inc.
Richmond, California
www.geowingmapping.com
Member Since: 12/2016

GPI Geospatial Inc.
Orlando, Florida
www.aca-net.com
Member Since: 1/1994

Halff Associates, Inc.
Richardson, Texas
www.halff.com
Member Since: 8/2021

Keystone Aerial Surveys, Inc.
Philadelphia, Pennsylvania
www.kasurveys.com
Member Since: 1/1985

Kucera International
Willoughby, Ohio
www.kucerainternational.com
Member Since: 1/1992

L3Harris Technologies
Broomfield, Colorado
www.l3harris.com
Member Since: 6/2008

Merrick & Company
Greenwood Village, Colorado
www.merrick.com
Member Since: 4/1995

Nearmap
South Jordan, Utah
www.nearmap.com
Member Since: 6/2023

NV5 Geospatial
Sheboygan Falls, Wisconsin
www.quantumspatial.com
Member Since: 1/1974

Pickett and Associates, Inc.
Bartow, Florida
www.pickettusa.com
Member Since: 4/2007

PixElement
Belmont, Michigan
https://pixelement.com
Member Since: 2/2017

Riegl USA, Inc.
Orlando, Florida
www.rieglusa.com
Member Since: 11/2004

Robinson Aerial Surveys, Inc.(RAS)
Hackettstown, New Jersey
www.robinsonaerial.com
Member Since: 1/1954

Sanborn Map Company
Colorado Springs, Colorado
www.sanborn.com
Member Since: 10/1984

Surdex Corporation
Chesterfield, Missouri
www.surdex.com
Member Since: 12/2011

Surveying And Mapping, LLC (SAM)
Austin, Texas
www.sam.biz
Member Since: 12/2005

T3 Global Strategies, Inc.
Bridgeville, Pennsylvania
https://t3gs.com/
Member Since: 6/2020

Towill, Inc.
San Francisco, California
www.towill.com
Member Since: 1/1952

Woolpert LLP
Dayton, Ohio
www.woolpert.com
Member Since: 1/1985

SUSTAININGMEMBER**BENEFITS**

Membership

- ✓ Provides a means for dissemination of new information
- ✓ Encourages an exchange of ideas and communication
- ✓ Offers prime exposure for companies

Benefits of an ASPRS Membership

- Complimentary and discounted Employee Membership*
- E-mail blast to full ASPRS membership*
- Professional Certification Application fee discount for any employee
- Member price for ASPRS publications
- Discount on group registration to ASPRS virtual conferences
- Sustaining Member company listing in ASPRS directory/website
- Hot link to company website from Sustaining Member company listing page on ASPRS website
- Press Release Priority Listing in *PE&RS* Industry News
- Priority publishing of Highlight Articles in *PE&RS* plus, 20% discount off cover fee
- Discount on *PE&RS* advertising
- Exhibit discounts at ASPRS sponsored conferences (exception ASPRS/ILMF)
- Free training webinar registrations per year*
- Discount on additional training webinar registrations for employees
- Discount for each new SMC member brought on board (Discount for first year only)

*quantity depends on membership level

Landsat's Enduring Legacy

Pioneering Global Land Observations from Space

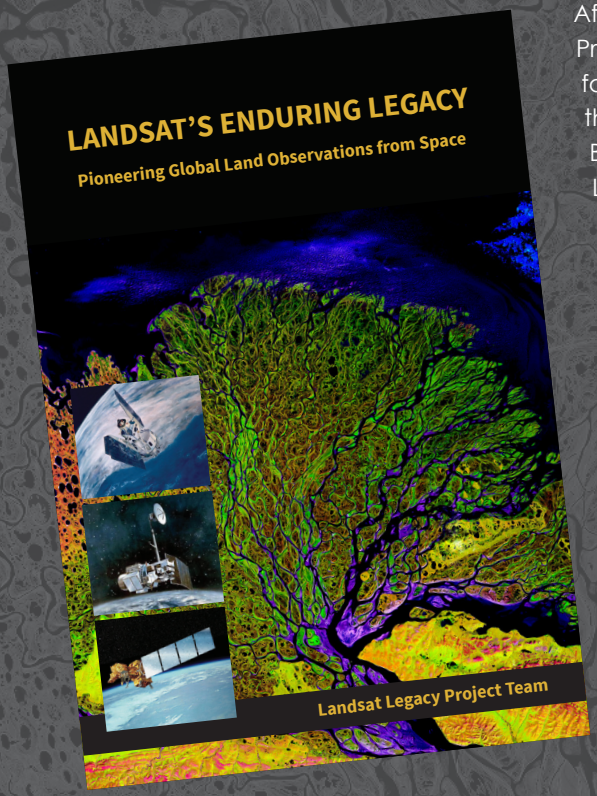

After more than 15 years of research and writing, the Landsat Legacy Project Team published, in collaboration with the American Society for Photogrammetry and Remote Sensing (ASPRS), a seminal work on the nearly half-century of monitoring the Earth's lands with Landsat. Born of technologies that evolved from the Second World War, Landsat not only pioneered global land monitoring but in the process drove innovation in digital imaging technologies and encouraged development of global imagery archives. Access to this imagery led to early breakthroughs in natural resources assessments, particularly for agriculture, forestry, and geology. The technical Landsat remote sensing revolution was not simple or straightforward. Early conflicts between civilian and defense satellite remote sensing users gave way to disagreements over whether the Landsat system should be a public service or a private enterprise. The failed attempts to privatize Landsat nearly led to its demise. Only the combined engagement of civilian and defense organizations ultimately saved this pioneer satellite land monitoring program. With the emergence of 21st century Earth system science research, the full value of the Landsat concept and its continuous 45-year global archive has been recognized and embraced. Discussion of Landsat's future continues but its heritage will not be forgotten.

The pioneering satellite system's vital history is captured in this notable volume on Landsat's Enduring Legacy.

Landsat Legacy Project Team

Samuel N. Goward
Darrel L. Williams
Terry Arvidson
Laura E. P. Rocchio
James R. Irons
Carol A. Russell
Shaida S. Johnston

Landsat's Enduring Legacy

Hardback. 2017, ISBN 1-57083-101-7

Member/Non-member	$48*
Student Member	$36*

* Plus shipping

Order online at

www.asprs.org/landsat

asprs THE IMAGING & GEOSPATIAL INFORMATION SOCIETY